

Master's thesis

**Design, fabrication and characterization
of InGaAs microdisk cavities on silicon
substrates toward III-V-on-Si lasers**

III-V-on-Si レーザに向けたシリコン基板上 InGaAs
マイクロディスクキャビティの設計、作製と特性評価

By

Fu Yufeng

Department of Electrical Engineering and Information systems,
The University of Tokyo

August 2014

Supervisor:
Prof. Yoshiaki Nakano

Contents

Chapter 1 Introduction	1
1.1 Si photonics.....	1
1.2 III-V integration on Si	3
1.2.1 Monolithic III-V integration	3
1.2.2 Hybrid III-V integration	4
1.3 Microdisk laser and whispering gallery mode.....	5
1.4 Research motive	6
Chapter 2 Improvement of MC-SA growth of InGaAs on Si	7
2.1 MOVPE growth.....	7
2.2 Micro-channel selective-area MOVPE growth of InGaAs on Si.....	8
2.3 Fabrication of template for growth	10
2.4 Micro-channel selective-area MOVPE growth of InGaAs on Si with thick SiO ₂ mask	12
2.4.1 InAs nucleation	12
2.4.2 InAs layer growth	14
2.4.3 InGaAs layer growth.....	15
2.5 Summary.....	17
Chapter 3 FDTD simulation of microdisk cavities	18
3.1 FDTD method	18
3.2 Crystalwave simulation	20
3.3 Hollow hexagon.....	22
3.4 Ring and Circular disk.....	25
3.4.1 Ring	25
3.4.2 Circular disk.....	27
3.5 Thickness dependence	31
3.6 Numerical analysis.....	32
3.7 Summary.....	33
Chapter 4 Fabrication	34
4.1 Sputtering.....	34
4.2 EB writing.....	35
4.2.1 Pattern design.....	35
4.2.2 EB writing condition.....	36
4.2.3 Alignment issue.....	37

4.3 ICP dry-etching.....	38
4.4 Result.....	40
Chapter 5 Photoluminescence measurement.....	43
5.1 PL system.....	43
5.1.1 Setup	44
5.1.2 Basic flow of measurement	44
5.2 Result.....	45
5.2.1 InGaAs island.....	45
5.2.2 Hollow hexagonal cavity.....	48
5.2.3 Ring cavity.....	50
5.2.4 Circular disk cavity.....	52
5.3 Summary.....	55
Chapter 6 Summary	56
Reference	58
List of publications.....	60
List of equipment	61
Acknowledgement	62

Chapter 1 Introduction

1.1 Si photonics

For a long time, the performance of computing system has been improved by downscaling the integrated circuit minimum feature size. It enables basic IC blocks to work at higher frequency level and provide higher speed. Besides, more blocks can be integrated in the same area, which can improve the total computation performance. However, the miniaturization in size is also followed by smaller wires and more complex connection between blocks. It brings problems as parasitic capacitance, contributing to signal propagation delay. These problems become inevitable as we consider the interconnect between chips. In high-performance computing system the delay due to the communication between the chips becomes comparable, or even over the computational delay itself, are known as interconnect bottleneck.

Silicon Photonics Technology[1] is a new approach to make optical devices on silicon platform and transfer data by using light through waveguides instead of electrical signals over copper cables. Rapid development in Si photonics over last decades has been driven not only by the need of low power consumption, high functionality photonic integrated circuits, but also by its potential in solving the bottleneck in chip to chip communications[2, 3].

Thanks to the endeavor of scientists and engineers, we have witnessed an explosion of breakthroughs in this area, such as Ge-on-Si lasers[4], demonstration of ultrafast Si modulators[5], development of commercial Si-based CMOS photonics for high-speed interconnects[6] and so on. A series of silicon photonic components have been successfully demonstrated, e.g. multiplexer, modulators and detectors, all providing comparable performance to their conventional counterparts. Besides, all of silicon photonics can be made using existing semiconductor fabrication techniques.

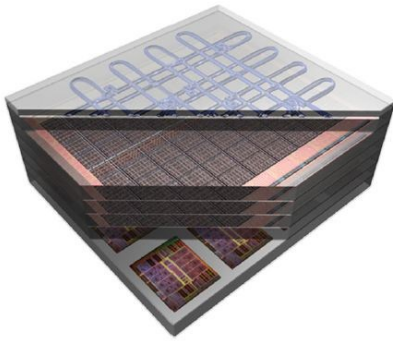


Fig. 1-1. Optical interconnection networks[7]

Fig. 1-1 shows an example of a monolithic silicon stack with the bottom plane for chip multiprocessors, several planes in the middle for local memory and the top plane for the photonic interconnection network, which comprises all the silicon photonic devices. Communication between planes is purely electrical using high-density through-silicon via technology. When a core from a chip multiprocessor wishes to communicate with another core, it sends the electrical data packet to the photonic plane, where it is converted into the optical domain using silicon photonic modulators. This optical data packet is then routed through the photonic network-on-chip to its target destination using silicon photonic switches. The optical packet is converted back into electrical domain using photodetectors.

In spite of those exciting progress, a major obstacle for large-scale silicon based electronic and photonic integration is the absence of an efficient light source, because of the indirect band-gap of silicon. At the very beginning of exploration in this area, the fundamental problem in realizing stimulating emission in Si was understood: optical transition must obey the law of conservation of energy and momentum. As an indirect band-gap material, free-carrier absorption, Auger recombination and indirect recombination exist simultaneously, resulting in little photon emission. Current research mainly focuses on approaches including: stimulated Raman scattering[8], rare-earth doping[9], monolithic III-V integration[10] and hybrid laser technologies[11].

Despite being fundamentally limited by an indirect band-gap and low mobility, Si exhibits a number of important properties that make it a good substrate for lasers. First, its simple atomic and crystal structure make it possible to make wafers with incredible purity and defect density. Second, fabrication of Si photonic components is compatible with complementary metal-oxide-semiconductor (CMOS) technology. Furthermore, Si

has a high thermal conductivity, which is a very useful characteristic for an active device substrate. Its high-quality native oxide---SiO₂, serves as a good waveguide cladding material and rare earth-doping host material, making silicon waveguide with significantly lower propagation loss than its counterparts.

1.2 III-V integration on Si

Among several approaches to realize light source on Si, monolithic III-V integration and hybrid III-V integration are regarded as two promising solutions.

1.2.1 Monolithic III-V integration

Many III-V compounds, such as GaAs, InGaAs, InP, have demonstrated good properties such as direct bandgap and high refractive index. The critical challenge of utilizing III-V materials to integrate laser on silicon is growing high-quality III-V materials on silicon substrates. As we known, lattice mismatch, thermal expansion coefficient mismatch, polarity mismatch exist between Si and III-V materials, which can cause defects at the interface and bending while cooling down.

	Si	Ge	GaAs	InP	InAs	GaP
Lattice constant [nm]	0.357	0.357 (4.2%)	0.357 (4.1%)	0.359 (8.1%)	0.361 (11.6%)	0.355 (0.4%)
Bandgap [eV]	1.11	0.66	1.43	1.35	0.36	2.26
Thermal expansion ratio [$\times 10^{-6}K^{-1}$]	2.4	5.5	6.0	4.5	5.19	5.3
transmission	Indirect	Indirect	Direct	Direct	Direct	Indirect

Table 1-1. Properties of semiconductors[12]

To overcome this challenge, people have taken approaches, including special surface treatment, strained superlattices, low-temperature buffers and growth on patterned substrates to reduce the dislocation density. One example is InGaAs nanopillar lasers grown on Si with GaAs shell using the bottom-up self-organized technique as shown in Fig.2. (a)[13]. It has an extreme small footprint of 0.34 μm^2 and unique helically propagating cavity mode. Another interesting example is Ge on Si epitaxial growth[4]. Despite being indirect band-gap material, its energy gap from the top of valence band to Γ valley is close to the actual band-gap, increasing the chance of radiative recombination. This kind of band-gap engineering has built a new way to realize integrated lasers on Si. The optically pumped Ge-on-Si laser operating at room temperature is demonstrated in Fig.2. (b).

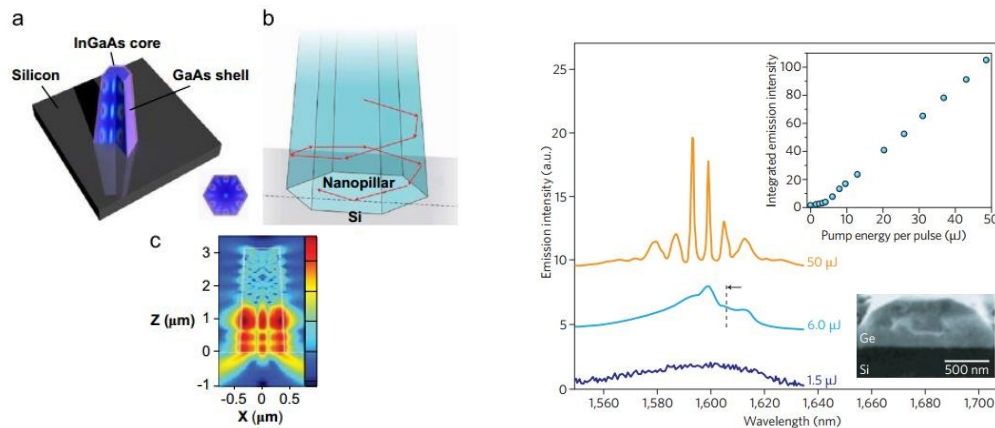


Fig.1-2 (a) Scheme of a nanopillar laser monolithically integrated onto Si. (b) Optically pumped Ge-on-Si laser demonstrating CW operation at room temperature.

1.2.2 Hybrid III-V integration

Instead of growing single materials on Si, hybrid lasers are made by a combination of several materials. This strategy shares the same idea with wafer-bonding, which means that we combine compound semiconductors with SOI substrates. As we know, compound semiconductors have superior gain characteristics, while SOI can be the perfect material for waveguides. By combining the advantages of each material, we can achieve high functionality as well as flexibility. Following the demonstration of first hybrid Fabry–Pérot lasers[14, 15], a variety of cavity devices were soon fabricated on hybrid platform, including DFB lasers[16] and DBR lasers[17] and micro-ring lasers[11].

One example of hybrid III-V-on-Si platform recently developed by Ghent University possesses device structure in Fig 3, though the III-V material and the Si waveguide perform relatively independent functions[18]. A relatively thick low-index medium between III-V and Si prevents photons generated in the III-V active region from coupling into the Si waveguide instantly. Lasing is achieved through the gain provided by a III-V active region and reflection at the etched laser facets. As the stimulated emission leaves the edge of the laser diode, an optimal adiabatic inverted taper structure is employed to achieve good coupling efficiency and fabrication tolerance.

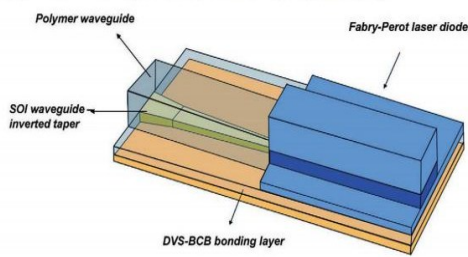


Fig. 1-3 Schematic of the layout of the optical coupling scheme for efficient and fabrication tolerant coupling between a bonded Fabry-Perot laser diode and an underlying SOI waveguide circuit using an inverted adiabatic taper approach.

1.3 Microdisk laser and whispering gallery mode

Semiconductor microdisk lasers with whispering-gallery modes (WGMs) are of great interest for their potential applications in optical interconnects [19] and bio-sensing [20]. By designing the microdisk shape, size or material composition, it can be tuned to support a spectrum of optical modes with required polarization, frequency and emission patterns. Fig. 1-4 shows a typical structure of microdisk laser. Laser part can be integrated by either epitaxial growth or wafer bonding on SOI. When the laser is operating, part of the evanescent wave is coupled to the waveguide passing beneath the microdisk, therefore being extracted from this laser.

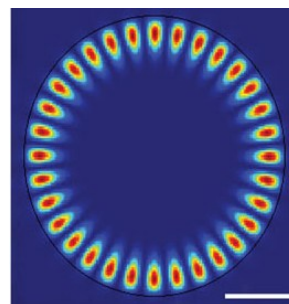
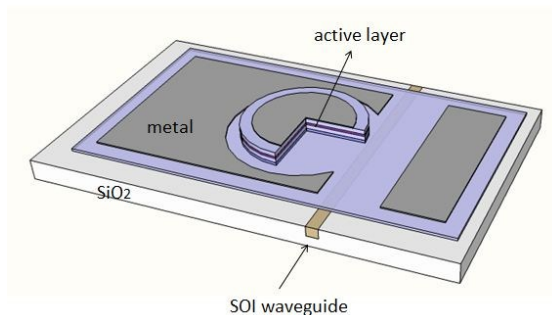


Fig. 1-4 structure of a typical microdisk laser Fig. 1-5 Whispering gallery modes[21]

The concept of whispering-gallery modes (WGM) was first introduced and developed by Lord Rayleigh in 1910 and 1914 to elucidate why sound waves travel more efficiently along the inside wall of a circularly shaped structure[22]. Nowadays, it is feasible to consider WGM in device having the physical dimension at micro and nanometer scales. As we know, total internal reflection of light at interface between a

dielectric material and air can reduce the propagation loss significantly. Microdisk cavities usually have symmetric shapes like ring and disk, which can the confine the light within the structure very well.

Due to the minimal reflection losses and very low material absorption, microdisk cavities with WGM have exceptionally high Q factor, compared to values for Fabry-Perot cavities. The extraordinary high Q factor of WGM leads to high energy density, narrow resonant wavelength range, and potentially downscaling of the size. These properties make microdisk cavities with WGM of great interest for lasers and sensors.

1.4 Research motive

To this end, we have recently developed a novel micro-channel selective-area metal-organic vapor phase epitaxy (MC-SA MOVPE) technique to grow a hexagonal InGaAs microdisk array monolithically on a silicon substrate[23]. Strong photoluminescence at 1.55- μm wavelength was observed [24]. On the other hand, however, lasing operation could not be achieved due to the absence of high- Q WGM inside such a hexagonal microdisk. Rapid carrier diffusion into the indium-rich center of the disk has also prohibited efficient pumping to the lasing mode.

This research aims to the design, fabrication and characterization of InGaAs microdisk cavities towards III-V integrated lasers on Si substrate. We have proposed three types of microdisk structures, including hollow hexagonal cavity, ring cavity and circular disk cavity. The main content of each chapter are listed below.

Chapter 2 Improvement of MC-SA MOVPE growth of InGaAs on Si.

Chapter 3 FDTD simulation of microdisk cavities

Chapter 4 Fabrication

Chapter 5 PL measurement

Chapter 6 Summary

Chapter 2 Improvement of MC-SA growth of InGaAs on Si

Our lab has developed micro-channel selective-area MOVPE growth for III-V monolithic integration on Si. In particular, we have successfully growth uniform InGaAs island on Si(111) using micro-channel selective area MOVPE growth[25]. However, the quality and uniformity decrease as we tried growth on template with thick SiO₂ layer (1 μ m), which is a prerequisite condition for optical device.

In this chapter, the basics of micro-channel selective-area growth of InGaAs on Si are introduced. Besides, we mainly focus on the improvement of quality and uniformity of InGaAs islands on Si template with thick SiO₂ mask by MC-SA MOVPE growth

2.1 MOVPE growth

In the Metalorganic vapour phase epitaxy (MOVPE) technique, precursors (gas) with their relative partial pressures are combined at high temperature in the reactor to cause a chemical interaction, resulting in the deposition of materials on the substrate. The materials include group III-V elements such as GaAs, InP, InAs, GaN and with some dopants.

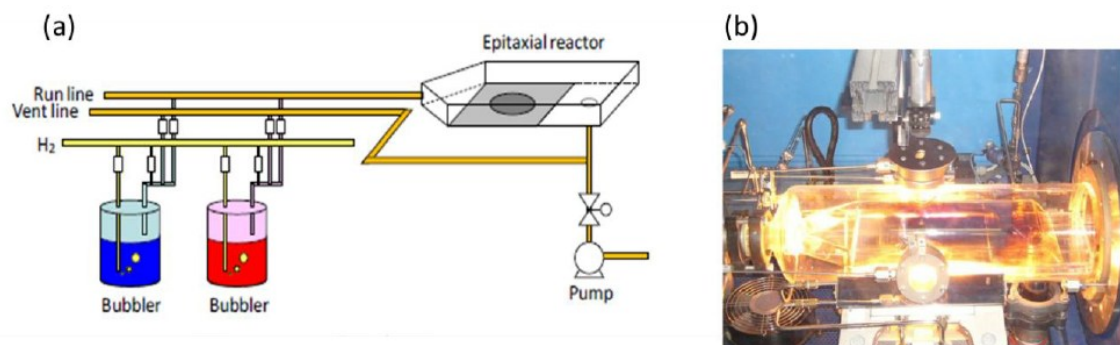


Fig. 2-1 (a) Schematic of MOVPE system, (b) Picture of reactor chamber

Though the whole MOVPE system is very complicated including gas mixing, cooling system, pneumatic system, exhaustion system, safety control and so on, the main part is plotted in Fig. 2.1. The reactor consists of an outer-tube, a liner-tube, a susceptor, and a back-plate. Usually these precursors are in liquid in room temperature. They go through

bubblers where carrier gas hydrogen is saturated, turning into gas phase and flow to next step. Run line and Vent line is set to control the partial pressure of precursor against carrier gas. We can tune each gas flow by switching the working condition of both lines. The precursor and hydrogen in Run line would flow into epitaxial reactor. Two or multiple kinds of reactant gas will react in the reactor chamber, separating into active units by the elevated temperature, and reacting at the surface of template.

2.2 Micro-channel selective-area MOVPE growth of InGaAs on Si

In spite of the difference between Si and III–V such as lattice constant and thermal expansion coefficients, our lab has successfully growth uniform InGaAs island on Si(111) using micro-channel selective area MOVPE growth.

Micro-channel selective area growth limits the growth area by the use of amorphous SiO₂ masks. III-V semiconductors grow only on the Si surface, therefore we can obtain the epilayer at the desired position at one growth. Moreover, restriction of the growth area to a small size of around a few μm is essential for obtaining a single-grained epitaxial island.

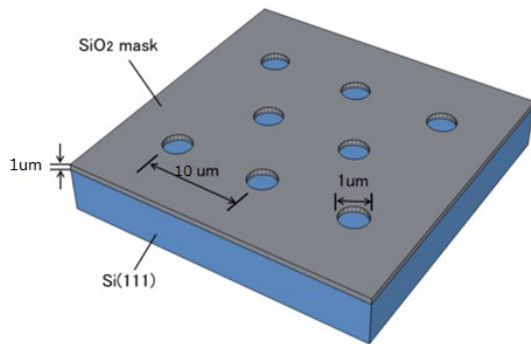


Fig. 2-2 Template for InGaAs micro-channel selective area growth

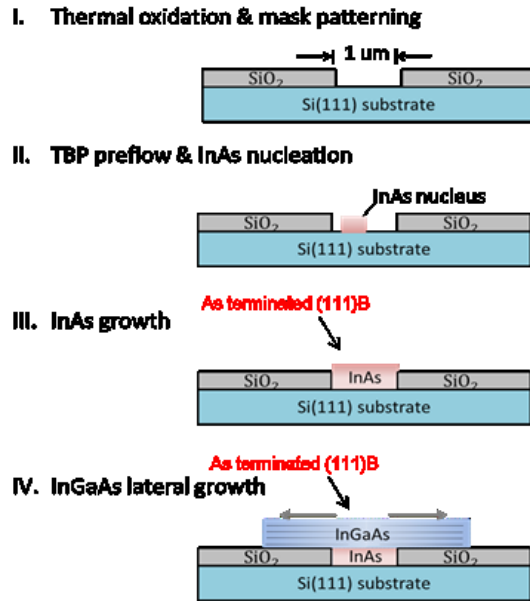


Fig. 2-3 scheme of InGaAs micro-channel selective-area growth

After preparation for template and followed by thorough cleaning, we set templates on top of susceptor and moving into reactor chamber. Three stages including nucleation, InAs layer growth and InGaAs layer growth are programmed as recipe for MC-SA growth.

As our plan is to fabricate optical components on such platform, good isolation between the optical device and substrate is required, due to their similarity in refractive index. Although the refractive index of InGaAs may change as the Ga percentage changes, we can assume that it is approximately 3.4, which is very close to the refractive index of Si substrate (3.3). In general, optical community believes that with an isolation larger than 1 μm, portion of evanescent wave coupled to the substrate could be negligible or in other word, not strong enough to compromise the measurement result. Considering this issue, we set the growth template with 1 μm SiO₂ mask.

Previous lab members have achieved high quality and uniformity of InGaAs with MC-SA MOVPE growth on the Si with 100nm SiO₂. Parameters including area size[26], pitches between each area, TBP pre-flow[27] have been studied. However, when thickness of SiO₂ mask increases to the level of 1 μm, this recipe is not applicable only because of the change in duration of InAs layer growth, but also in nucleation condition. In addition to change of growth recipe, template fabrication is also turn out to be different.

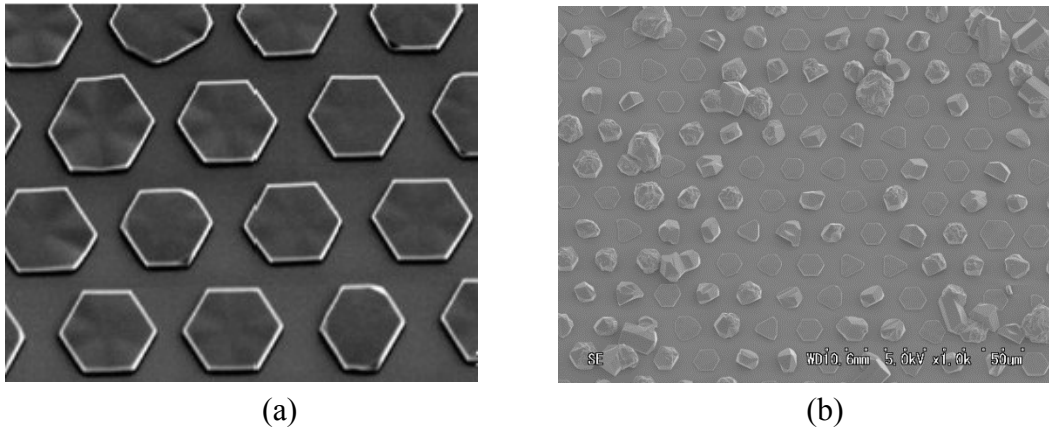


Fig. 2-4 InGaAs microdisk on Si by MC-SA MOVPE with template having (a) 100nm SiO₂ mask (b) 1μm SiO₂ mask

2.3 Fabrication of template for growth

Here we will introduce the fabrication of template for micro-channel selective-area growth of InGaAs. The quality property of template may influence the growth result significantly.

Previous study shows that III/V material has preference to grow on Si with (111) crystal orientation. Therefore 4-inch Si(111) wafer is used as raw material. Wet oxidation is followed to make a fine SiO₂ layer. The thickness of SiO₂ layer is measured to be 1.2μm by Dektak. Designed pattern is drawn onto 4-inch Si wafer by EB (electro-beam) lithography in Takeda.

Designed 0.8μm_10μm_fu.bef pattern has an area of 8mm*10mm, consists of 459*699 hole pairs with hole diameter of 0.8μm and pitch of 10μm. The diameter and pitch are deliberately chosen based on preliminary study. Other marks are also added into this pattern for alignment and convenience consideration.

Resist	spincoating	bake
OAP	3000rpm 30s	none
OEBR112	3000rpm 60s	2min 110°C
Espacer 300Z	3000rpm 60s	10min 110 °C

Table 2-1. EB resist condition

After EB writing, 90s Post exp bake is required under 110°C. The development is taken with 2 steps:

30 seconds in Water to remove Espacer and 60 seconds in 2.38% TMAH solution. Finally, 90 seconds under 110 °C of Post bake is taken to solidify the EB resist.

The previous template used for growth employed SiO₂ mask of 100nm, and wet etching only was used to etch the patterned holes. However, in this case, given 1μm thickness, the isotropic etching property of wet etching will enlarge the hole size. The growth condition is sensitive to the size, especially the nucleation stage. Actually EB resist layer will be partly lift-off, which means that it can no longer work as the mask to make the selectively etching happen. If the duration is longer than 5min, for example, all of the area begins to be exposed to BHF, and their etching rate is almost the same.

Dry-etching is introduced in this process. Unlike wet-etching, EB resist can function perfectly for SiO₂ etching mask. But dry etching also has its own issues. Usually CHF₃ does little to Si, but actually it can do small damage to Si surface, which is detrimental for the nucleation. Besides, etching trench is found at the edge of the etching area, due to larger gas flux at the edge comparing to the center. These issues make the tricky question: how can we etching to the place where it is close to Si surface but should not touch Si surface. We make a dummy with exact the same pattern, and expecting to have the same dry-etching condition at such irregular localized area. By observing the etching result of dummy, we can estimate the etching rate for trench or the bottom. After proper duration of dry-etching based on the etching rate from dummy test, 2min wet-etching of SiO₂ is taken in order to remove the residues of SiO₂ at the bottom. We can check the bottom of hole from the top or cut it to observe the cross-section by SEM.

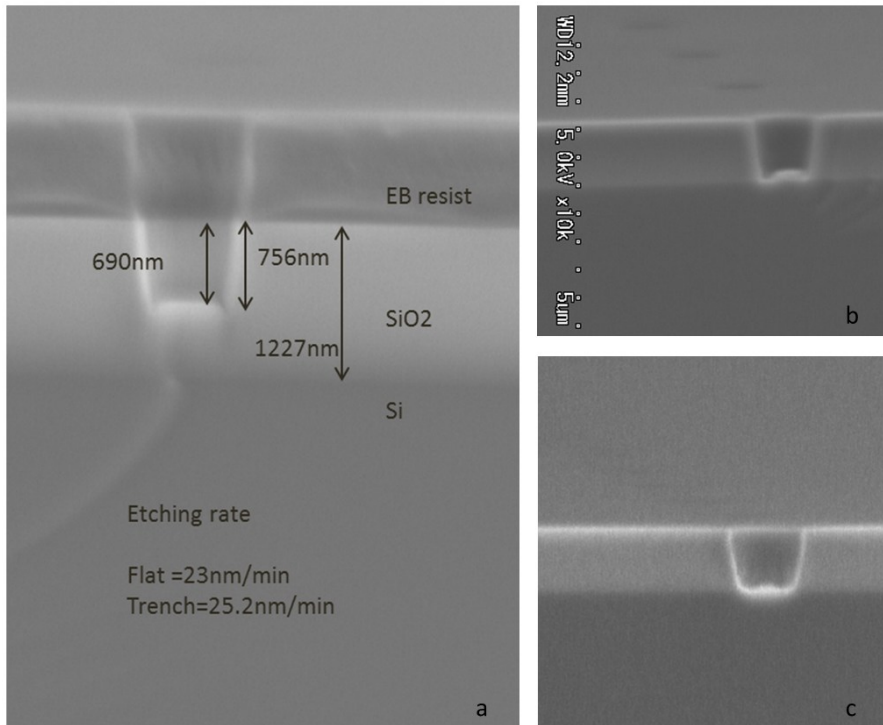


Fig. 2-5 a. Dummy template for SiO₂ etching rate test after 30min CHF₃ dry-etching; b. Template after 45min CHF₃ dry-etching and 2min BHF; c. Template after 45min CHF₃ dry-etching and 2min+3min BHF

Based on the result, uniformity of template is difficult to achieve. This is because in the dry-etching process, taking 4-inch wafer for example, the center part has higher etching rate than edge part. Then we have to compensate that low etching rate by increasing the time in wet-etching, which make the SiO₂ mask of those templates thinner and holes larger. Our strategy here is to take two adjacent templates (A, B) as one unit, assuming their spatial vicinity can give relatively uniform properties.

In the stage of conditioning, for example the nucleation stage, we can assume that the condition we have tested for A is at least valid for its counterpart B.

Templates for MOVPE growth have to be cleaning thoroughly following three steps. It is recommended that the cleaning should be conducted one day before the growth, to avoid the re-oxidizing process in Si surface of micro-channels.

1. Aceton with ultrasonic excitation, rinse in IPA, then in DI
2. 10min in Piranha (H₂O₂:H₂SO₄=1:3) at 140°C, double rinse in DI, then 10 rinse in running DI.
3. 40s in 0.5% BHF, double rinse in DI

The step above is to remove organic particles, metal, and surface oxidation respectively.

2.4 Micro-channel selective-area MOVPE growth of InGaAs on Si with thick SiO₂ mask

As we have introduced in 2.2, in general, we can separate the growth by three steps:

1. InAs nucleation
2. InAs layer growth
3. InGaAs layer growth

The ideal growth procedure should be as follow:

Step 1: Easy for nucleation on Si

Step 2: Difficult for nucleation on Si, easy for InAs vertical deposition on III/V

Step 3: Easy for InGaAs lateral deposition on III/V

We would like to analysis and discuss the growth result of each step below.

2.4.1 InAs nucleation

InAs nucleation as the first step is of vital importance. In 20 seconds, single tiny nucleus of InAs should deposit on each micro-channel Si surface. Usually III/V will deposit on Si surface randomly, forming an amorphous epilayer. But by restrain of the growth area to a circle with a radius of around a few μm , we are able to obtain a single-grained epitaxial island. The growth results indicate that besides the nucleus size, “single nucleus” in each area is the most important point we care about. Let’s assume two nucleus in the same selective-area. In the stage 2, InAs could deposit on each InAs nucleus, they compete with each other and boundary emerges. In this case, after stage 2, we will usually find irregular shape of InAs pillars, which would grow into poli-crystal in the stage 3. Nucleation with nucleus number larger than two will have the same problem. In some rare cases multi-nucleus could grow into good hexagons, due to their locations satisfying the properties of InAs crystal. However, this condition is not preferred.

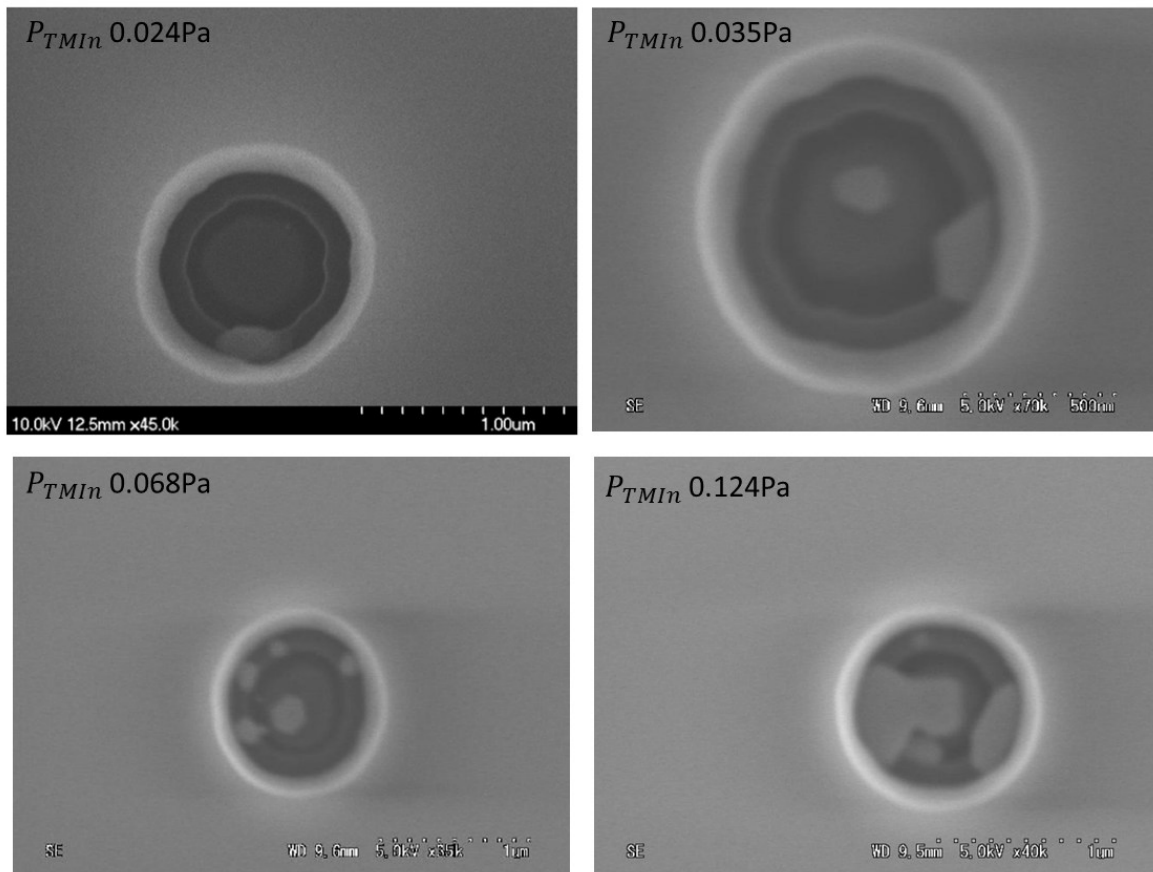


Fig. 2-6 Nucleation dependence to partial pressure of TMIn.

Fig. 2-6 shows that the probability of InAs nucleus formation is related to P_{TMIn} in

the selective-area. The partial pressure of *TMIn* is changing from 0.024Pa, 0.035Pa, 0.068Pa and 0.124Pa. P_{TMIn} 0.068Pa is the previous condition, and based on this result, multiple nucleus occur and may develop into poly-crystal in next stage. We can conclude here that P_{TMIn} 0.024Pa is optimal in nucleation condition for 1um thick mask MC-SA MOVPE growth.

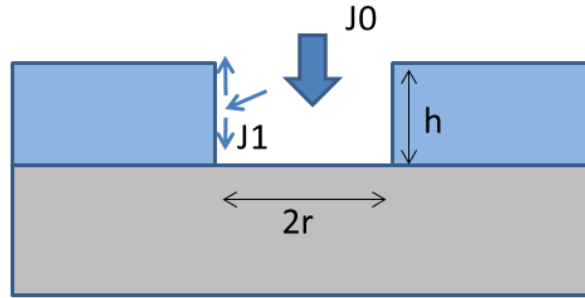


Fig. 2-7 Scheme of InAs nucleation in micro-channel

The structure of single selective area is shown above in Fig. 2-7. If we consider the gas flux in this area, J_0 to be the flux vertical to Si surface from gas phase precursor source, J_1 represents the gas flux to the wall of SiO₂ mask, and a portion of that will flow to the Si surface to participate the nucleation process. The thickness of SiO₂ mask is marked as h . r is the radius of the circular area. We can calculate the amount of precursor accumulated in this area per second by

$$\frac{dN}{dt} = JS = \pi r^2 J_0 + \alpha 2\pi r h J_1$$

Here α is a coefficient between 0 and 1. While divided by the area πr^2 ,

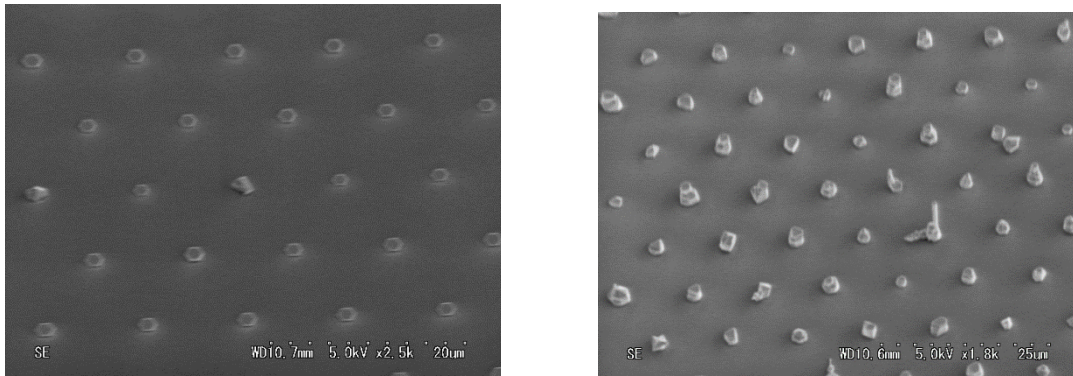
$$\frac{dC}{dt} = J_0 + \frac{\alpha 2h J_1}{r}$$

If we assume that J_0 , J_1 remain the same while changing SiO₂ thickness h , we can find the increase in thickness prone to the accumulation of precursor, which increase the susceptibility to nucleation. This analysis is consistent with our experiment result. We can predict from this derivation that shrinking the area could possibly have the same effect as increasing the thickness.

2.4.2 InAs layer growth

In stage 2, we increase the partial pressure of both *TMIn* and *TBAs*. In this stage, first each area is filled with InAs on lateral direction. As the area is very limited, soon the surface will be covered by InAs epilayer. Then InAs layer begins to grow on vertical

direction due to the restriction of the growth area. We note here that the duration of stage 2 is appropriate when the InAs layer grows a few hundred nano-meters higher than the SiO₂ mask. The dependence of InAs layer height to time is not clear, but based on our test result, 43 minutes 30 seconds are viable for a mask thickness about 1 μ m. If the InAs layer is not taller enough to exceed the SiO₂ mask, then normally it turns into poly-crystal; while if the InAs layer is much taller than the SiO₂ mask, normally the size of the hexagon would shrink, which could be explained by the increase the exposed surface area given the certain amount of precursors in localized atmosphere.



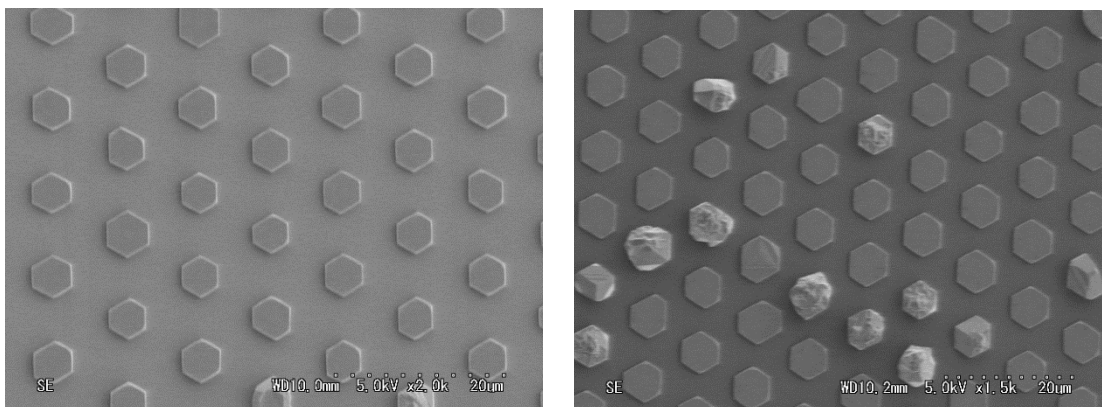
a. Single nucleus

b. Multiple nucleus

Fig. 2-8 43min30s InAs layer growth after 20s nucleation.

2.4.3 InGaAs layer growth

There is not much to mention about the third stage. Based on growth result, we find the size of InGaAs hexagon is dependent on duration of this stage. Usually we can expect InGaAs hexagon with side length of 2.5 μ m by 80min. When we increase the duration of this stage, the size does increase, but not necessarily proportional. Previous growth result shows that even change the duration by 160min, the increase is modest. Here we assume 120min is longer enough. It gives InGaAs hexagon islands with side length of 3 μ m.



(a)80min InGaAs

(b)120min InGaAs

Fig. 2-9 Time dependence of InGaAs layer stage

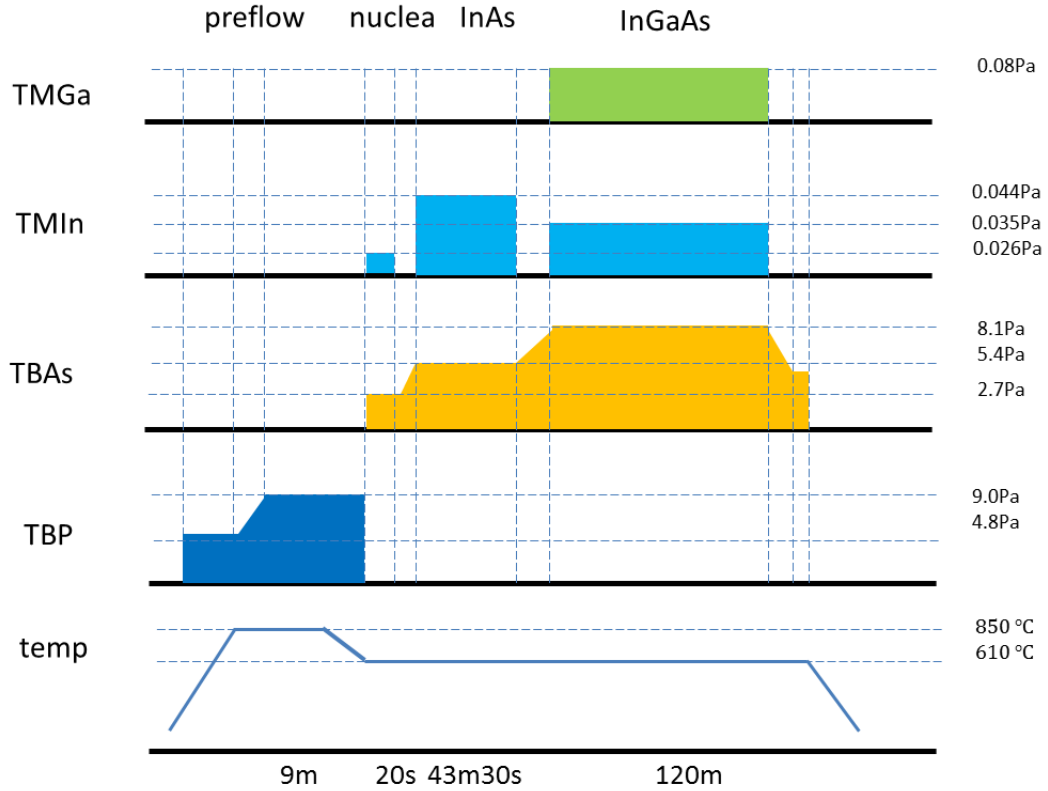


Fig. 2-10 Flow rate of each precursor at different steps.

Finally Fig. 2-10 shows the entire growth recipe, which includes the partial pressure of different sources and temperature in each stage. If we compare with the previous recipe, we can note that the main difference lies in nucleation stage. Fig. 2-11 shows that good quality and uniformity of InGaAs array is achieved by our recipe.

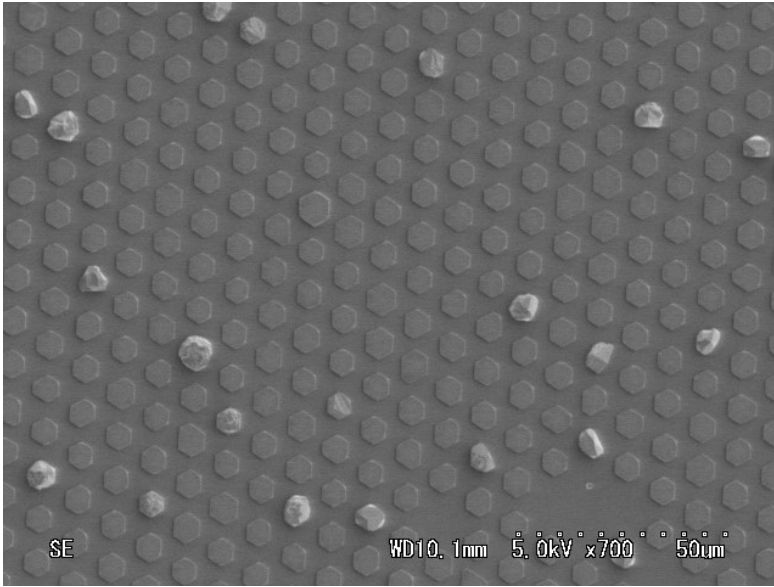


Fig. 2-11 InGaAs microdisk on Si by MC-SA MOVPE with template having 1um SiO₂ mask

2.5 Summary

We have introduced the basic flow of MC-SA MOVPE growth of InGaAs on Si. Starting from previous recipes, we have studied and confirmed the growth condition of each step, and optimized the nucleation condition for 1um thick SiO₂ mask Si template. By adjusting the nucleation condition, we have drastic improvement in uniformity and quality. These InGaAs samples can be used as material platform for my next design and fabrications.

Chapter 3 FDTD simulation of microdisk cavities

In chapter 2, we have developed a novel micro-channel selective-area metal-organic vapor phase epitaxy (MC-SA MOVPE) technique to grow a hexagonal InGaAs microdisk array monolithically on a silicon substrate. In this chapter, the CrystalWave includes a highly efficient FDTD (finite difference time domain) engine is used to simulate the propagation of light through the designed cavities. We have proposed cavities including hollow hexagon structure, ring structure and circular disk structure. Resonant wavelength and its mode field distribution at different geometry sizes are demonstrated, which give insights to the design and fabrication of microdisk cavities.

3.1 FDTD method

FDTD is a numerical analysis method for modeling field distribution and evolution in certain structure. When we take a look at Maxwell's differential equations, the change in the E-field in time (the time derivative) is dependent on the change in the H-field across space (the curl).

$$\nabla \times \mathbf{E} = -\frac{\partial \mathbf{B}}{\partial t} \quad (3-1)$$

$$\nabla \times \mathbf{H} = \frac{\partial \mathbf{D}}{\partial t} + \mathbf{J} \quad (3-2)$$

This results in the basic FDTD time-stepping relation that, at any point in space, the updated value of the E-field in time is dependent on the stored value of the E-field and the numerical curl of the local distribution of the H-field in space. Similar manner appears when we consider H-field in time. At any point in space, the updated value of the H-field in time is dependent on the stored value of the H-field and the numerical curl of the local distribution of the E-field in space. The idea is that we separate the space into Yee cells as below in Fig. 3-1[28], setting time into time steps.

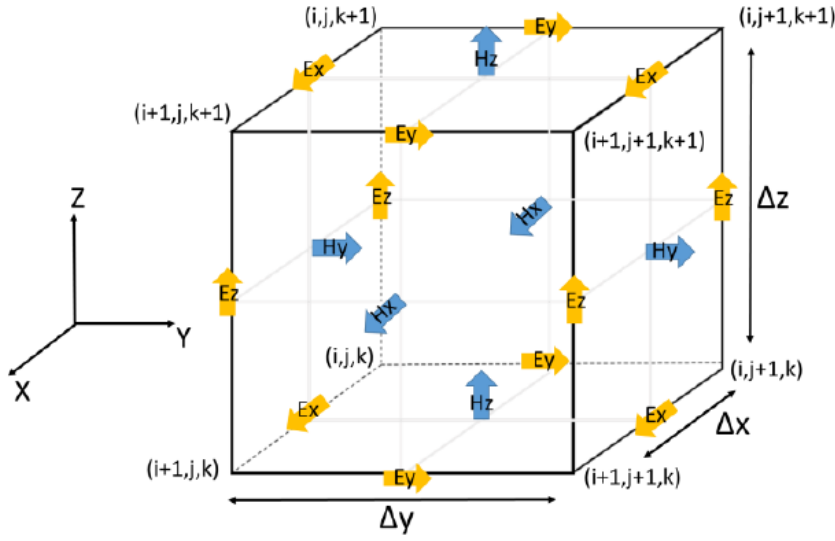


Fig. 3-1 Illustration of a standard Yee cell used for FDTD, about which electric and magnetic field vector components are distributed.

In order to elucidate the relation of E and H in such cells, we need to consider the differential equation below, take x axis for example:

$$\frac{\partial F}{\partial x} = \frac{F(x+\frac{\Delta x}{2}, y, z, t) - F(x-\frac{\Delta x}{2}, y, z, t)}{\Delta x} \quad (3-3)$$

$$\frac{\partial F}{\partial t} = \frac{F(x, y, z, t+\frac{\Delta t}{2}) - F(x, y, z, t-\frac{\Delta t}{2})}{\Delta t} \quad (3-4)$$

We rewrite the form of F as

$$F(x, y, z, t) = F^n(i, j, k) \quad (3-5)$$

Here i, j, k refer to the spatial position of cell, n refers to the time step of each condition.

$$\frac{\partial F}{\partial x} = F^n\left(i + \frac{1}{2}, j, k\right) - F^n\left(i - \frac{1}{2}, j, k\right) \quad (3-6)$$

$$\frac{\partial F}{\partial t} = F^{n+\frac{1}{2}}(i, j, k) - F^{n-\frac{1}{2}}(i, j, k) \quad (3-7)$$

We substitute E and H into F,

$$\frac{\partial E}{\partial x} = E^n\left(i + \frac{1}{2}, j, k\right) - E^n\left(i - \frac{1}{2}, j, k\right) \quad (3-8)$$

$$\frac{\partial E}{\partial t} = E^{n+\frac{1}{2}}(i, j, k) - E^{n-\frac{1}{2}}(i, j, k) \quad (3-9)$$

$$\frac{\partial H}{\partial x} = H^n \left(i + \frac{1}{2}, j, k \right) - H^n \left(i - \frac{1}{2}, j, k \right) \quad (3-10)$$

$$\frac{\partial H}{\partial t} = H^{n+\frac{1}{2}}(i, j, k) - H^{n-\frac{1}{2}}(i, j, k) \quad (3-11)$$

E and H in adjacent cells can be calculated using equation (3-8) and (3-10). It has been proved that this description is also true when multiple dimensions are considered.

By applying $B = \mu H$, $D = \varepsilon E$, $J = \sigma E$ to the equation (3. 1), (3. 2), we have

$$\frac{1}{\varepsilon} \nabla \times H = \frac{\partial E}{\partial t} \quad (3-12)$$

$$\frac{1}{\mu} \nabla \times E = \frac{\partial H}{\partial t} \quad (3-13)$$

Then,

$$\frac{1}{\mu} \nabla \times E^n = H^{n+\frac{1}{2}}(i, j, k) - H^{n-\frac{1}{2}}(i, j, k) \quad (3-14)$$

$$\frac{1}{\varepsilon} \nabla \times H^n = E^{n+\frac{1}{2}}(i, j, k) - E^{n-\frac{1}{2}}(i, j, k) \quad (3-15)$$

Iterating the E-field and H-field updates results in a marching-in-time process wherein sampled-data analogs of the continuous electromagnetic waves under consideration propagate in a numerical grid stored in the computer memory. The concept of FDTD simulation is to solve the Maxwell's equation and determine E,H field at every grid within the computational domain.

3.2 Crystalwave simulation

CrystalWave includes a highly efficient FDTD (finite difference time domain) engine is used to simulate the propagation of light through the designed cavities. In CrystalWave, the basic flow of one complete FDTD simulation is as follows:

1. Creating a device (geometry)
2. Setting up the device (material)
3. Adding excitors
4. Adding sensors
5. Setting FDTD parameters
6. Perfoming a 3D FDTD calculation
7. Ploting sensor flux

Algorithm

Crystal Wave uses a Yee cell algorithm for FDTD calculations. With this algorithm, the

grids for the electric and magnetic fields are staggered, with electric fields defined at the center of the 6 cube faces and magnetic fields defined at the center of 12 cube edges; the curl of each electric field is calculated from the 4 surrounding magnetic fields.

Time steps

The duration of calculation, i.e. the number of time steps for which the FDTD engine should evolve the field. The duration should be set to a value large enough to allow the evolution of the field over the period of interest.

Central wavelength

This parameter is introduced to calculate the complex dielectric constant from specified refractive index and loss at the specified central wavelength.

Grid

The FDTD engine assigns a material to each grid cell, known as discretization. The FDTD further assigns electric and magnetic field amplitudes to each grid cell for each time step of the calculation. It is strongly recommended that set grid parameter matching the periodicity of the lattice and maintaining the symmetry of the structure at the same time. Grid size must be sufficiently small to represent the smallest feature of the device.

Boundary condition

To achieve reflection-free truncation of the computational space, the FDTD engine surrounds the device with a uniaxial PML. For three-dimensional calculations, it is added on all sides of the structure. The PML thickness and boundary condition can be overridden on one or more faces of the device using overrides property. For example, certain faces can be overridden with PEC or PMC conditions.

Sensor minimum wavelength

This parameter determines that how the FDTD engine stores the fields in the sensors in the frequency domain. A range of wavelength, which you are interested in, can be specified. This reduces the amount of memory required for the calculation

Sensor time undersample

The sensor time undersample FDTD parameter determines how the FDTD engine stores the fields in the sensors in the time domain.

3.3 Hollow hexagon

Here, we propose a novel hollow hexagonal InGaAs microdisk cavity and numerically investigate its mode properties.

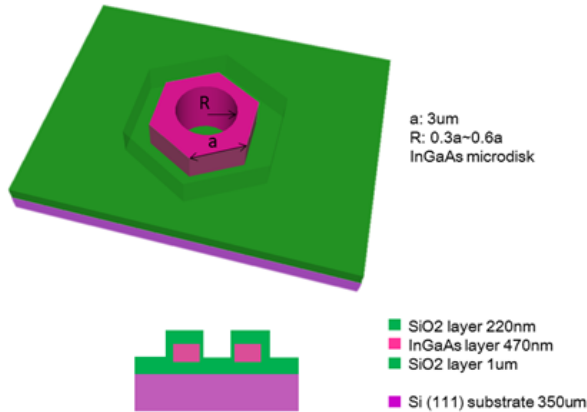


Fig. 3-2 Schematic of the hollow InGaAs hexagonal microdisk cavity

Fig. 3-2 shows the schematic of the hollow InGaAs hexagonal microdisk cavity proposed in our research. A 470-nm-thick InGaAs ($n=3.4$) microdisk sits on top of a 1- μm -thick SiO_2 ($n=1.45$) layer on the Si substrate ($n=3.48$), and the entire structure is passivated by a thin SiO_2 layer. The InGaAs microdisk has a hexagonal outer shape with a side width $a = 3 \mu\text{m}$. At the center of the disk, we introduce a small etched hole with a radius of R .

We carried out the mode analysis of the hollow hexagonal InGaAs microdisk cavity with increasing hole radius using the fully vectorial three-dimensional finite-difference time-domain (FDTD) method. The resonant wavelength and the cavity Q factor of different modes were recorded in the wavelength range from 1.47 μm to 1.6 μm .

Fig. 3-3 shows the resonant wavelength of different modes plotted as a function of R/a . Among several modes, three modes having the highest Q values are specified and traced throughout the simulation. For convenience, we denote them as Mode 1 (around 1.55 μm), Mode 2 (around 1.58 μm), and Mode 3 (around 1.49 μm) as shown in Fig. 2. The Q values of respective modes are plotted as a function of R/a in Fig. 3-3.

From Fig. 3-3 and Fig. 3-4, we see that in the range of $0 < R/a < 0.42$, only Mode 1 is present as a moderately high-Q mode. Its wavelength remains nearly unchanged while the Q factor drops gradually from 371 to 38 with increasing R . When R/a exceeds 0.42, however, Mode 2 and Mode 3 emerge and their Q factors increase rapidly

with increasing R . They reach their maximum values of 2280 at $R/a = 0.48$ for Mode 2 and 3574 at $R/a=0.49$ for Mode 3. Both of these modes decay at $R/a > 0.50$, and only moderate Q factor is observed at larger R .

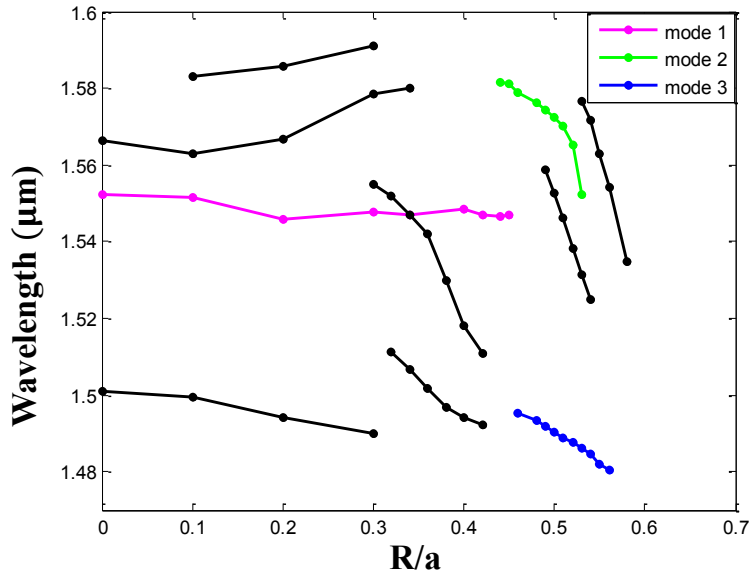


Fig. 3-3 Resonant wavelength of the cavity mode as a function of R/a . Three modes with the highest Q values are specified as Mode 1 (pink), Mode 2 (green), and Mode 3 (blue). Other modes with moderate Q are marked with black lines.

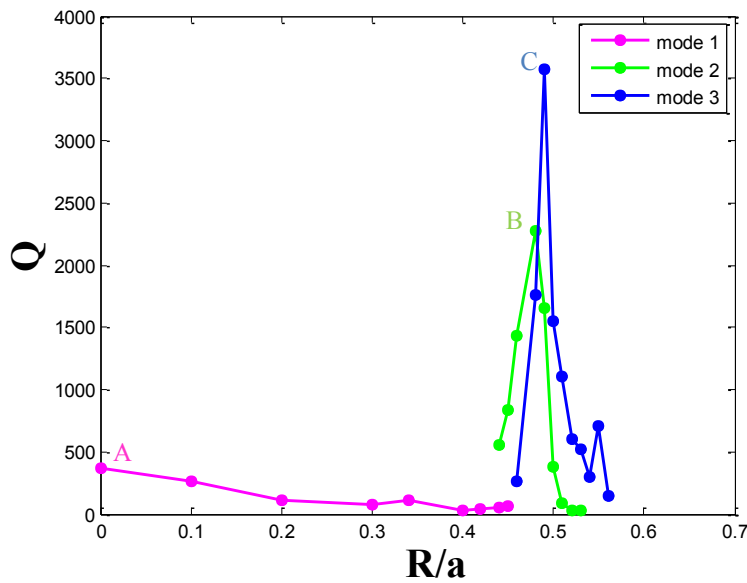


Fig. 3-4 Cavity Q factor of Mode 1 (pink), Mode 2 (green), and Mode 3 (blue) as a function of R/a .

To elucidate the high-Q properties of Mode 2 and Mode 3, which emerge only in the limited regime of $0.42 < R/a < 0.50$, we investigate the field profile of respective modes. Fig. 3-5 shows the mode field distribution for several different cases. When there is no hole [Fig. 3-5(a)], the mode field exhibits a complicated multi-mode interference pattern, resulting in a relatively low Q factor. On the other hand, Mode 2 at $R/a = 0.48$ [Fig. 3-5(b)] and Mode 3 at $R/a = 0.49$ [Fig. 3-5(c)] both resemble WGMs in circular microdisk lasers[29], where Mode 3 can be recognized as essentially identical to Mode 2 with merely higher mode index. Interestingly, for a larger hole radius with $R/a = 0.56$ [Fig. 3-5(d)], these quasi-WGMs disappear and the mode field exhibits multi-mode interference pattern again.

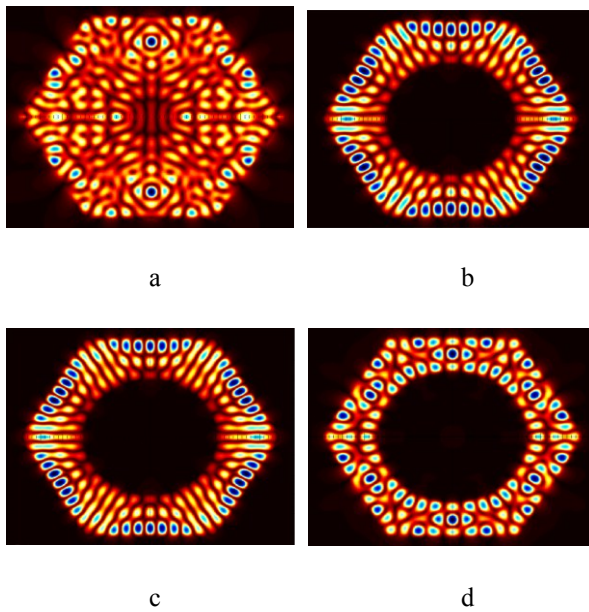


Fig. 3-5 Field profile of (a) Mode 1, $R/a = 0$ (no hole) at 1552 nm, (b) Mode 2, $R/a = 0.48$ at 1577 nm, (c) Mode 3, $R/a = 0.49$ at 1490 nm, and (d) $R/a=0.56$ at 1554 nm.

Although further study is required to clarify the mechanism, we could explain that when $0.42 < R/a < 0.50$, the phase interference condition is somehow satisfied at the six corners of the hexagonal disk, such that the propagating wave does not excite higher-order modes upon reflection at the edges. As a result, it propagates in a similar manner as a WGM inside a circular disk [Fig. 3-5 (b) and (c)]. In contrast, when $R/a < 0.42$ or $R/a > 0.50$, higher-order modes are excited upon each reflection, so that the mode field exhibits complicated interference pattern in the radial direction [Fig. 3-5 (a) and (d)]. Finally, we observe in Fig. 3-5 (b) and (c) that the optical intensity of the

quasi-WGM is concentrated mainly at the outside hexagonal boundary of the disk and less power is localized in the inner boundary. This feature is extremely attractive in practice, since we could utilize the naturally formed hexagonal facets during the SA-MC MOVPE process, and allow relatively large fabrication tolerance for the etched hole at the center.

3.4 Ring and Circular disk

Ring shape and circular disk shape are typical structure as microdisk cavity. Geometries as ring and circular can support WGM very well. Here we also propose InGaAs ring and circular disk cavity and numerically investigate its mode properties. Ring and circular disk cavity have the same layer information as hollow hexagonal cavity introduced in 3.3, because they are fabricated on the same InGaAs material platform.

3.4.1 Ring

We carried out the mode analysis of ring cavity with increasing inner radius in the center, while keeping the outside Radius constant to 2 μm . Fig. 3-6 (a) shows the top view of computation area. Fig. 3-6 (b) depicts the refractive index of each material at cross section. It is one quarter of a ring, with PEC boundary condition on both sides. InGaAs layer is marked red with refractive index of 3.4.

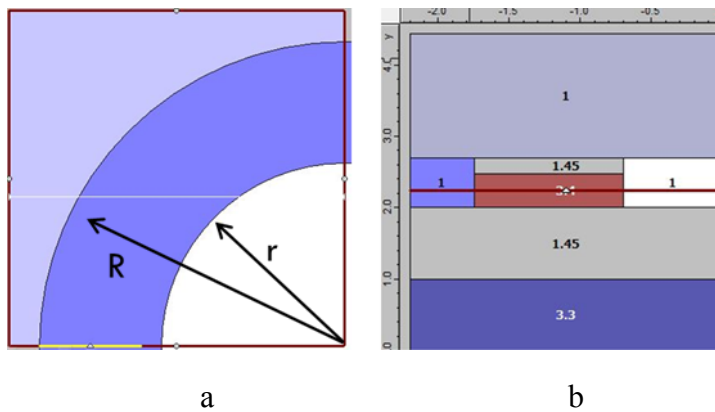


Fig. 3-6 3D FDTD simulation of ring structure (a) top view of computation area (b) refractive index of each material at cross section.

The resonant wavelength and the cavity Q factor of different modes were recorded in the wavelength range from 1.5 μm to 1.6 μm .

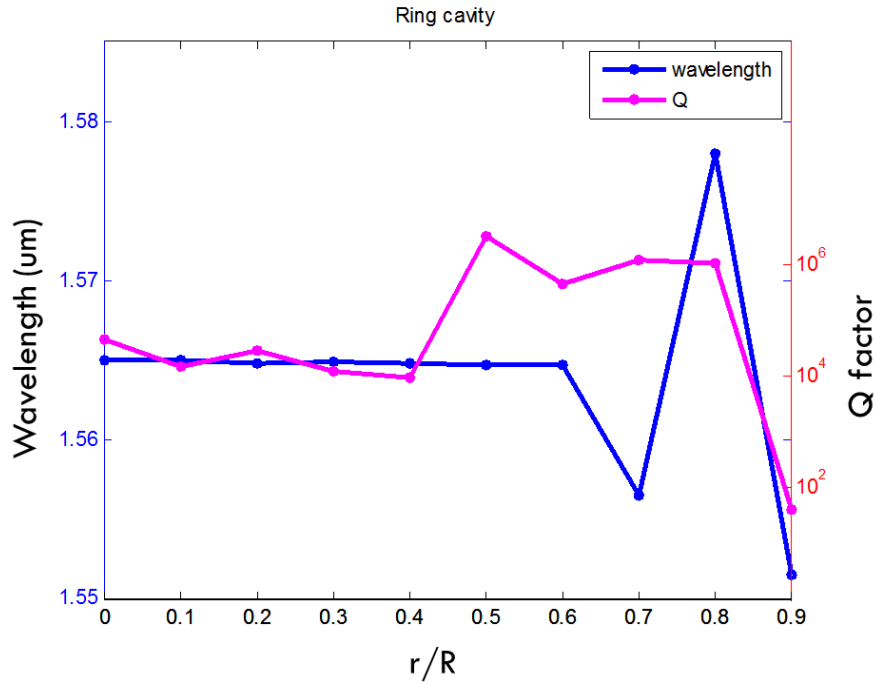


Fig. 3-7 Resonant wavelength and Q factor at different inner radius of the ring

From figure above, we find that ring structure has an extreme high Q compared with hollow hexagonal cavity in 3.2, varying from 10e3 to 10e6. Radius ratio represents the size of inner circle over outside circle. With higher radius ratio, the ring becomes thinner. It also to be noticed that resonant wavelength doesn't change much when the radius ratio is small. In the range 0 to 0.6, the resonant remains to be near 1.5650 um. The second mode is negligible until radius ratio larger than 0.5.

To elucidate the high-Q properties of each mode at different radius ratio, we investigate the field profile of respective modes. Figure 3-8 shows the mode field distribution for different radius.

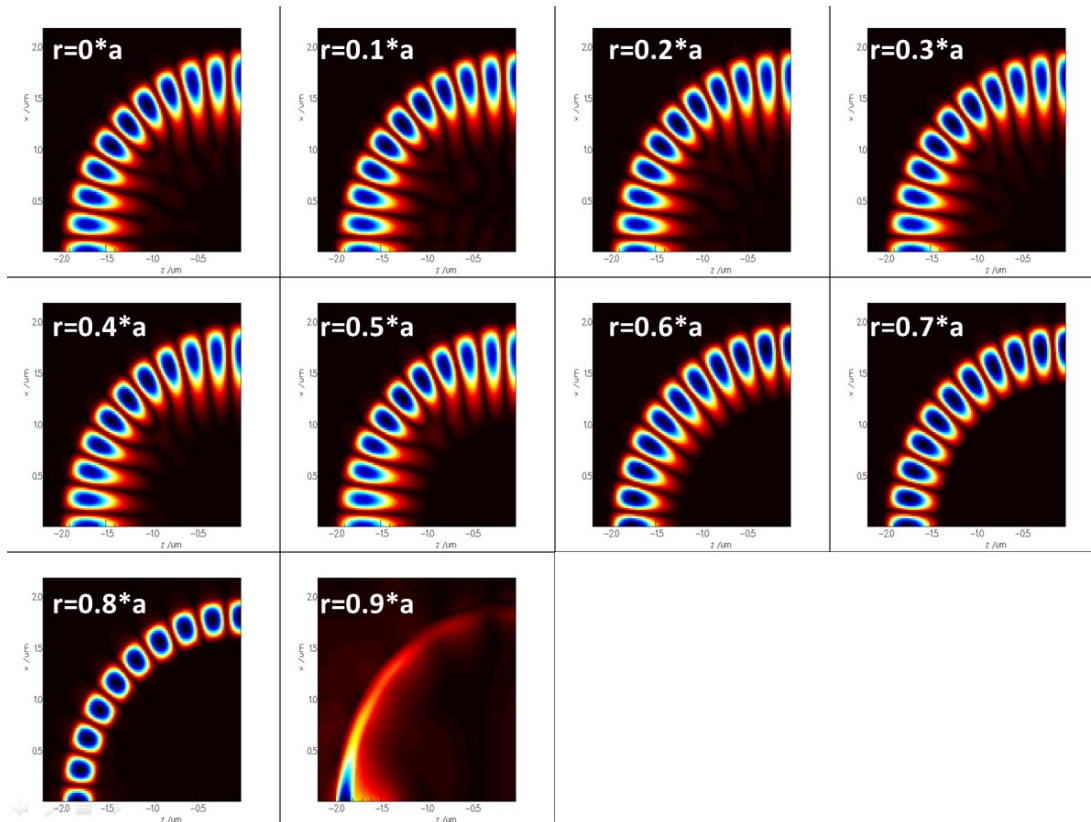


Fig. 3-8 Field profile of main modes at different inner radius of the ring.

From Fig. 3-8, we can find that in the range from 0 to 0.6, their mode field distribution resembles each other, which could be interpreted as they have the same mode. Since their mode field distribute at the outside of the ring, the size change in the inside affects them little. Until the ring become thinner than the bright blue spot, the inner facet of ring squeeze the field to outside, resulting in change in resonant wavelength. At $r=0.9*a$, the ring is too thin to support any modes. The Q factor increases can be explained by the decrease in mode numbers. As the ring becomes thinner, modes in azimuthal direction can be suppressed.

Another feather we notice from this dependence is that the disk can somehow represent the feature (resonant wavelength, Q factor) of the ring, if the ring is not too thin. Therefore, by analyzing the profile of circular disk, we can take a glimpse of the cavity properties of the ring with same outer size.

3.4.2 Circular disk

We also carried out the mode analysis of circular disk cavity with increasing radius. Fig. 3-9 shows the top view and cross section.

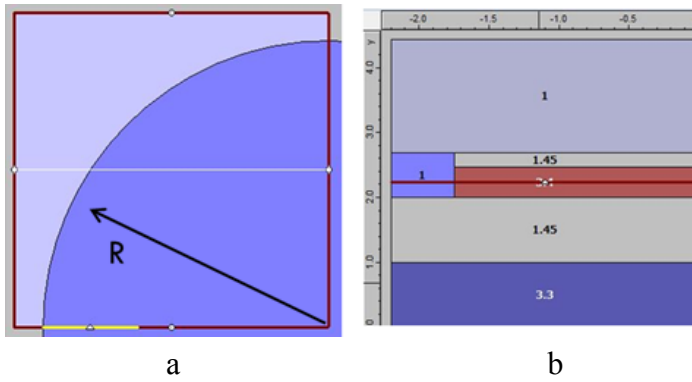


Fig. 3-9 3D FDTD simulation of circular disk structure (a) top view of computation area (b) refractive index of each material at cross section.

The resonant wavelength and the cavity Q factor of different modes were recorded in the wavelength range from 1.5 μm to 1.6 μm . It seems that circular disk has much more complex mode profile. Mode is scanned by top mode sensor. We find that both TE and TM mode are supported in this situation. The parameter E_y refers to TM mode, while H_y refers to TE mode.

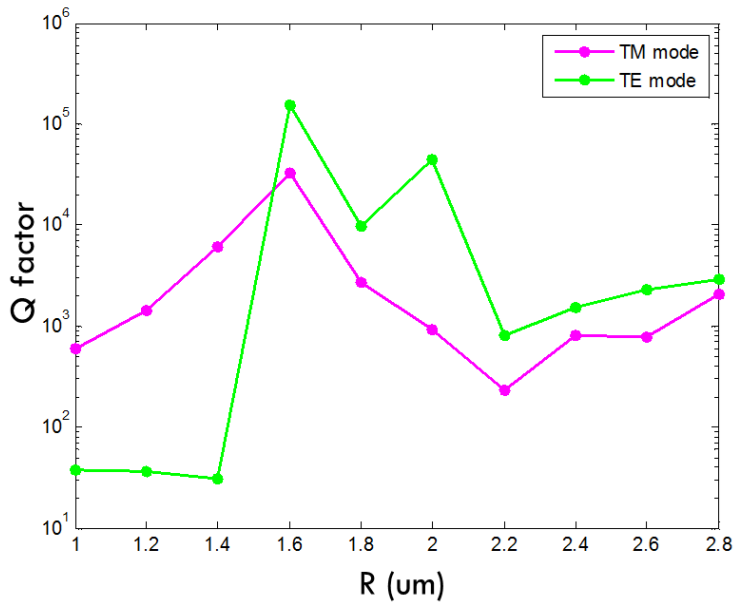


Fig. 3-10 Circular disk cavity Q factor of TM Mode (pink) and TE Mode (green) as a function of R .

First, we would like to demonstrate the resonant wavelength, Q factor and mode profile of TM modes.

Disk radius	w1	Q1
1	1.5037	597
1.2	1.5585	1454
1.4	1.5551	6108
1.6	1.5565	32809
1.8	1.5610	2723
2	1.5662	925
2.2	1.5486	230
2.4	1.5791	803
2.6	1.5293	777
2.8	1.5671	2071

Table 3-1 The resonant wavelength (TM) and Q factor at different radius of circular disk

From table above, we find that circular disk structure has a relatively high Q, varying from 10^2 to 10^4 . It is difficult to elucidate the dependence of Q factor and disk radius, as their wavelengths could relate to different modes. We can only state that from this simulation for the particular layer profile, the Q factor improvement is observed when disk radius increases from 1 μm to 1.6 μm , and then Q factor reaches its minimum at 2.2 μm , and begins to rise from 2.2 μm to 2.8 μm

We investigate the field profile of respective modes as well. Fig. 3-11 shows the mode field distribution for several cases.

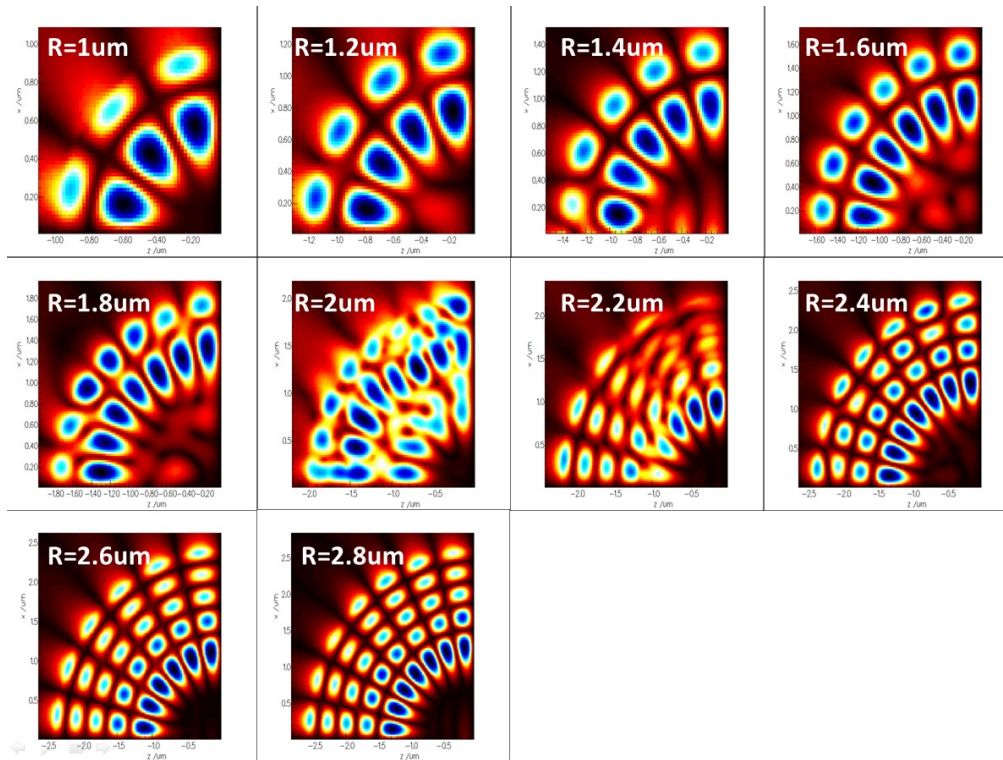


Fig. 3-11 Field profile of main TM modes at different radius of circular disk.

The high Q modes (R=1.6 um, Q=32809 and R=2.8 um, Q=2071) have a clear mode field distribution profile, while low Q point (R=2.2 um Q=230) has relatively blurred mode field distribution profile. Moreover, when the size of the disk increases, we can see the mode number in both radial and azimuthal direction increases.

Second, we would like to demonstrate the resonant wavelength, Q factor and mode profile of TE modes.

Disk radius	w1	Q1	w2	Q2
1.6	1.5139	1.57E+005		
1.8	1.5405	9620		
2	1.5650	44073		
2.2	1.5514	813		
2.4	1.5925	14911	1.5055	1516
2.6	1.5097	2334	1.5275	659
2.8	1.5461	2897	1.5244	1831

Table 3-2 Resonant wavelength (TE) and Q factor at different radius of circular disk

At some points, more than one resonant wavelength can be detected by top mode sensor at the range of 1.5um to 1.6um. Q factor changes from 10e2 to 10e5, and we

would like to mention that TE mode emerges only when the size of disk larger than 1.6um. Q factor reaches its top at 1.57e+005. At the radius range 1.6 um to 2.8 um, TE mode has relatively higher Q than TM mode, therefore being dominant in mode competition.

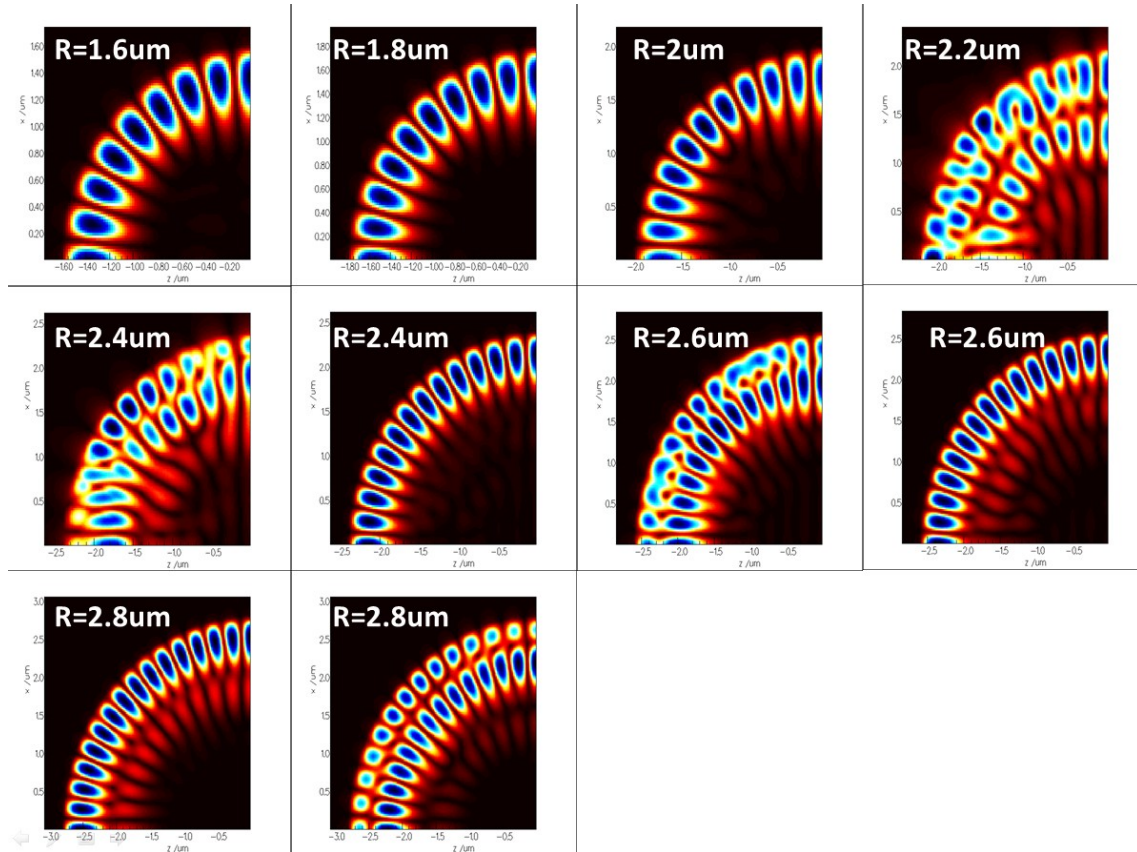


Fig. 3-12 field profile of main TE modes at different radius of circular disk.

By investigating the field profile of respective modes, we have the same conclusion: when the size of the disk increases, mode number in both radial and azimuthal direction increases. Besides, TE modes exhibit field distribution to be much more confined in the cavity, which could explain its high Q and dominance in mode competition.

3.5 Thickness dependence

For the structure above at point $R=0.48a$, we have simulated the dependence in thickness of isolation layer.

$R=0.48a$

thickness(nm)	w1	Q1	w2	Q2	w3	Q3
100	1.5747	35	1.4965	16	1.5557	31
300	1.5766	1652	1.4936	1686	1.5493	33

600	1.5765	1345	1.4932	2622	1.5012	11
1000	1.5767	2280	1.4934	1777	1.5511	34

Table 3-3 Resonant wavelength and Q factor at different thickness of SiO₂ layer of hollow hexagonal cavity at R=0.48a.

The resonant wavelength doesn't change much, but Q factor has obvious dependence in thickness. Though it turns out not to be linear, certain amount of isolation distance is necessary.

3.6 Numerical analysis

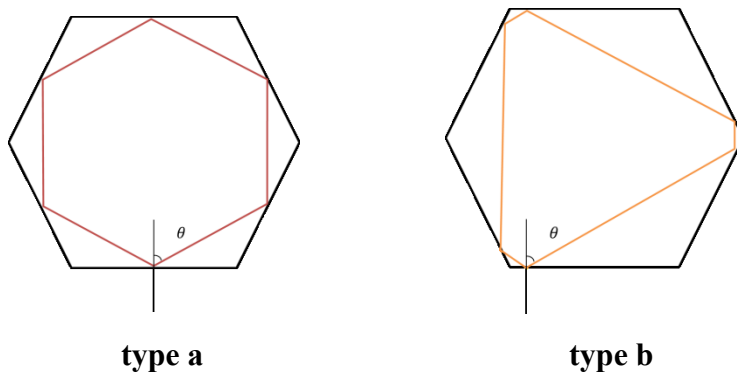


Fig. 3-13, a and b have same L despite their different optical paths.

A plane wave model has been applied to derive the relation between WGM number and wavelength. The idea is that a standing wave requires the total phase shift of the wave along its round trip to be an integer multiple of 2π . As seen in Fig. 3-13, a, a light wave completes one full circulation with 6 total internal reflections at the side wall of the hexagon, as the critical angle between these two material to be $0.354(20.3^\circ)$. Reflected light has an angle dependent and polarization dependent negative phase shift between the reflected and incident light.

- $$\phi(\theta) = -2 \tan^{-1} \left\{ \frac{\sqrt{\sin^2 \theta - \left(\frac{n_2}{n_1}\right)^2}}{\alpha \cos \theta} \right\}$$

$$\alpha = \begin{cases} 1 & TM \\ \frac{n_2}{n_1} & TE \end{cases}$$

- $nkL + 6 * \phi(\theta) = 2\pi N$ where N is an integer.

L corresponds to the length of optical path of one full circulation. As situation a and b in

Fig. 3-13, though their optical paths seem different, due to calculation they actually have same L. L is only a function of incident angle θ .

- $L = 3 * a * \frac{\sin\frac{2\pi}{3}}{\sin(\frac{\pi}{2}-\frac{2\pi}{3}+\theta)}$ where a is the side length of hexagon,

and θ is the incident angle. Here is $\frac{\pi}{3}$

The equation above enables us to calculate the relation between WGM number and wavelength.

λ	1.973	1.887	1.808	1.735	1.668	1.606	1.549	1.495	1.445	1.389
N	20	21	22	23	24	25	26	27	28	29

Table 3-4 Relation of WGM number and wavelength in hexagonal cavities at $a=3\mu\text{m}$.

3.7 Summary

In this chapter we have proposed cavities including hollow hexagon structure, ring structure and circular disk structure. Resonant wavelength and its mode field distribution at different sizes are demonstrated. Despite having low Q factor compared with ring structure and circular disk structure, hollow hexagonal cavity has advantages as it could utilize the naturally formed hexagonal facets during the SA-MC MOVPE process, and allow relatively large fabrication tolerance for the etched hole at the center. Ring cavity has an extreme high Q factor, which gain its maximum at r/R ratio at 0.6. We can get resonance information of the ring by analyzing a circular disk with the same outer Radius, as they have similar field distribution profile. And during the analysis, we also notice something very interesting such as circular disk has TM mode dominance at small radius, switch to TE mode at larger radius. We have also investigated the increases of mode number in both radial and azimuthal direction when the size of the disk increases. All of this information could give insights to the design and fabrication of microdisk cavities on this particular platform.

Chapter 4 Fabrication

In this chapter we would like to introduce the fabrication process after InGaAs MOVPE growth. As we mentioned in chapter 2, InGaAs hexagon islands with good quality and uniformity are obtained by optimizing the growth condition in each stage. Now we carry out our fabrication on this material platform.

There are three parts of my fabrication process after growth, including sputtering, EB lithography and ICP dry-etching. The process flow of hollow hexagonal InGaAs cavity are shown in Fig. 4-1. Ring cavity and circular disk cavity fabrication basically have the same process, except the patterns in EB writing.



Fig. 4-1 Process flow of hollow hexagonal InGaAs cavity on Si.

4.1 Sputtering

Anelva sputter machine is used for SiO₂ sputtering. SiO₂ sputter layer can be used as the etching mask of InGaAs etching after EB writing. In this sense, it is insensitive about the thickness of sputter layer. Sputter power is set to be 200W, and the sputter

time to be 30min. Usually this condition will give an approximate 220nm thick SiO₂ sputter layer, as it is tested by lab members. From some of the fabrication results, we find that the sputter layer is inhomogeneous at different places, such as the center and the angle of InGaAs hexagons. The angle of hexagon is not well covered because of the step difference between InGaAs and SiO₂ on template. In the later stage, we can see this effect that some hexagons suffer etching damage at the angles. Considering this effect, we adjust sputter time to be 40min, which gives us SiO₂ sputter layer a thickness about 300nm. By this adjustment, InGaAs hexagons are free from sputter damage at angles.

4.2 EB writing

EB writer is a crucial part of my fabrication as it determines the geometrical structure of my device. We expect accurate EB writing as we designed in the pattern, and with good alignment.

4.2.1 Pattern design

Three types of structures are designed and plotted with Klayout and saved as GDS file. Klayout is a good GDS plotting software which enables complex hierarchies and multiple layers. We have designed hole (hexagon with hole in center), circular disk and ring in one set, and making arrays with this set at different places. This strategy can deal with the problem of growth variability. Normally we cannot expect that all the area of template have the same high quality InGaAs hexagons with good uniformity. By making arrays of our patterns, we can reduce the probability that our patterns fall into some bad zones (moderate quality and uniformity).

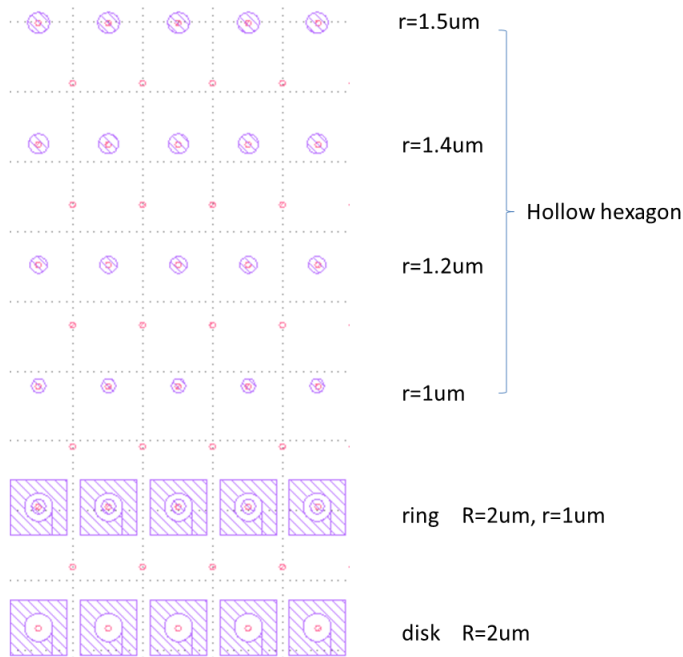


Fig. 4-2 Pattern design for EB writing. Red dots represent the micro-channel for InGaAs growth.

EB resist	Spin1	Spin2	bake
Primer	Slope 5s, 500rpm, 5s	Slope 5s, 3000rpm, 60s	none
ZEP-520A	Slope 5s, 500rpm, 5s	Slope 5s, 3000rpm, 60s	180°C, 3min

Table 4-1 Condition of EB resist

There are mainly two issues we care about: EB writing condition and alignment precision.

4.2.2 EB writing condition

At the field size of 100/20000, we can set exposure current and dose time before exposure. Generally, small beam current gives much more accurate EB writing, but meanwhile longer dose time is required. Resist sensitivity also makes difference here. Our experiment for conditioning suggests that exposure current 50pA and dose 0.5 us is optimal for our pattern. Current 50pA is used for fine structures.

EB lithography Dose time at 50 pA

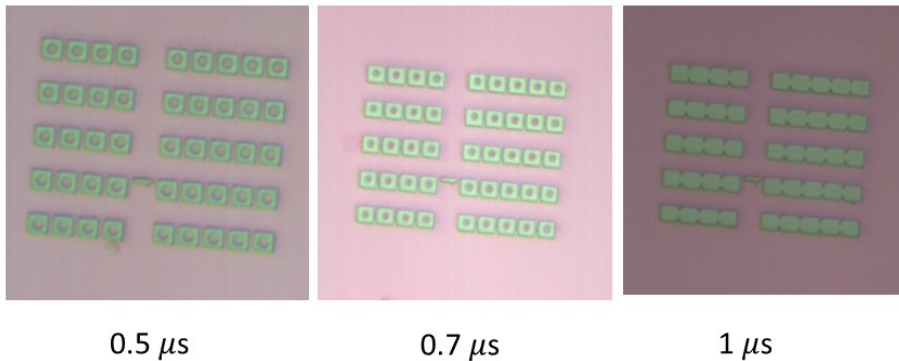


Fig. 4-3 EB writing result with different dose time at 50pA

One small issue I would like to mention here is when using Klayout designing patterns with subsets which is not simply-connected in topology, one extra line will emerge in that pattern. If it is parallel to the direction of writing, it will affect the EB writing, resulting in losing some parts of your design. One solution here is to rotate your pattern 90 degrees, keeping the extra line vertical to the direction of EB writing.

4.2.3 Alignment issue

Precise alignment is very essential for my design. As the sample composites of InGaAs islands rather than InGaAs layer, we need to put patterns precisely atop of these hexagons, where device is fabricated. Statistically speaking, InGaAs hexagon has a side length near 3 μ m. For structure of circular disk and ring, as their boundary does not exceed the InGaAs hexagonal island, it is ok. But this notion is on the base that all the InGaAs have the same Ga composition from the center to the edge in one single hexagon. Previous study shows that Ga composition increases as it grows far away from InAs center. This is also certified by PL with small spot size. In this sense, relatively good alignment is appreciated to realize the uniformity of Ga composition. Different from disk and ring structure, hole can be very sensitive to alignment. As we know that optical cavities, except some unidirectional lasers, usually employ structure with good symmetry. In our case, even though the WGM are supposed to emerge and propagate at the outer edge of hexagon, good alignment at the center is highly preferred.

Another issue we find in this stage is the width broadening of alignment marks. The alignment mark is designed to be 1 μ m in width. However, based on SEM, we have observed alignment mark broaden to be 6 μ m due to the growth of InGaAs. It could be

problematic as it is more difficult to determine the exact center of the alignment mark.

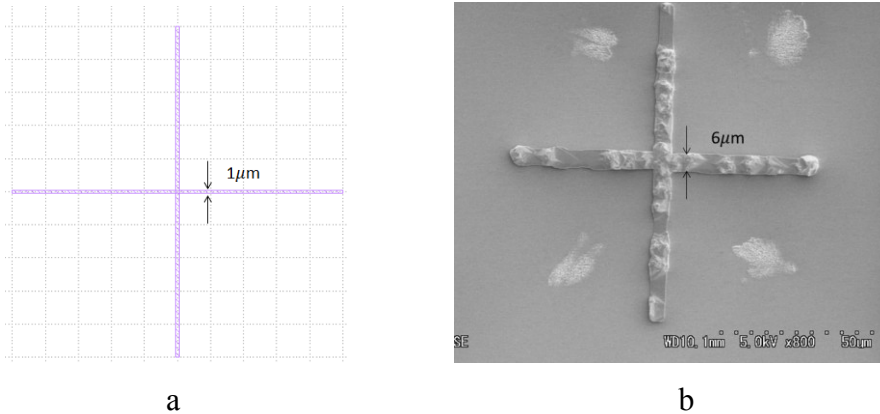


Fig. 4-4 Alignment mark (a)design in pattern (b) after InGaAs growth

One suggestion here is to design alignment with thinner lines, which could reduce the width of growth further. It should also be noted that some alignment is not symmetric due to the writing mechanism of EB machine. Therefore multiple alignment marks is also highly recommended to avoid some invalid alignment marks.

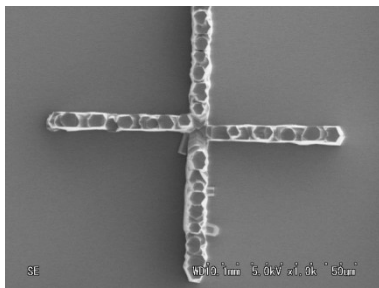


Fig. 4-5 Asymmetric alignment mark

4.3 ICP dry-etching

As we patterned EB resist on the material, we need to transfer that pattern to the SiO₂ sputtering layer. Therefore firstly we use CHF₃ to etch SiO₂. We mentioned in chapter 2 that the etching rate for SiO₂ dry-etching to be 23.3 ~ 25 nm/min. Given a thickness of 300nm SiO₂, we set the etching time to be 16min(3min longer to ensure the removal of SiO₂).

Gas Pressure	1.00 Pa	CH ₄ Flow Rate	0.00 sccm
Pressure Control	APC	H ₂ Flow Rate	0.00 sccm
	0 %	Ar Flow Rate	5.00 sccm
He Gas Select	ON	CF ₄ Flow Rate	5.00 sccm
He Gas Flow Rate	8.00 sccm	O ₂ Flow Rate	0.00 sccm
He Gas Inlet Time	0 min	BCL ₃ Flow Rate	0.00 sccm
Source Power	60 W	CL ₂ Flow Rate	0.00 sccm
Source Memory	No.1	Step Time	16min 0sec
Bias Power	25 W	Pressure Stability Time	0sec

Table 4-2 Recipe 4, condition 8 for SiO₂ etching

Then 10min Ashing is taken to remove the EB resist. If we skip this procedure, we will find that in high temperature, Cl₂ will react with EB resist and giving a black layer at the surface of sample.

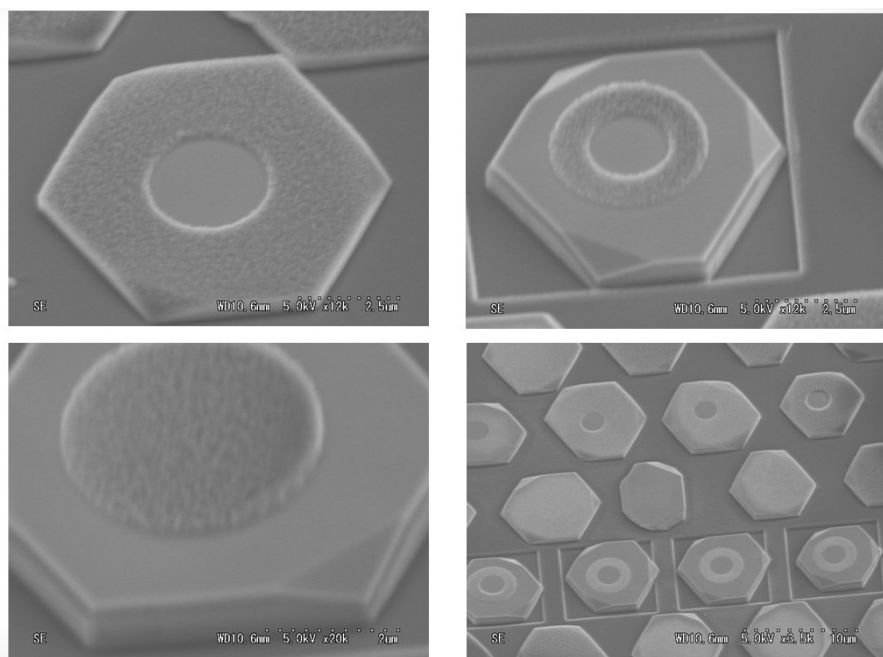


Fig. 4-6 SiO₂ mask on InGaAs island after CHF₃ etching

After checking SiO₂ patterns with SEM, we do Cl₂ etching at high temperature (220). High temperature is always required as the sample consists of Indium element. Two dummy runs are taken to stabilize the condition of etching chamber. Another tip is to surround sample with InP dummy chips, which could improve the stability of local gas flow. The etching rate cannot be exactly obtained from this etching test as 2min of Cl₂ etching has already reached the bottom of InGaAs hexagon. But give a thickness of InGaAs to be 470nm, we can at least assume that etching rate can be larger than 235 nm/min. We tried several recipes of Cl₂ etching, suggesting that Cl₂:Ar ratio=1.8:8.2 is optimal for InGaAs etching in our case.

Gas Pressure	2.00 Pa	CH4 Flow Rate	0.00 sccm
Pressure Control	APC	H2 Flow Rate	0.00 sccm
	0 %	Ar Flow Rate	8.20 sccm
He Gas Select	ON	CF4 Flow Rate	0.00 sccm
He Gas Flow Rate	8.00 sccm	O2 Flow Rate	0.00 sccm
He Gas Inlet Time	0 min	BCL3 Flow Rate	0.00 sccm
Source Power	140 W	CL2 Flow Rate	1.80 sccm
Source Memory	No.1	Step Time	2min 0sec
Bias Power	110 W	Pressure Stability Time	0sec

Table 4-3 Recipe 1, condition 2 for InGaAs etching at 220°C

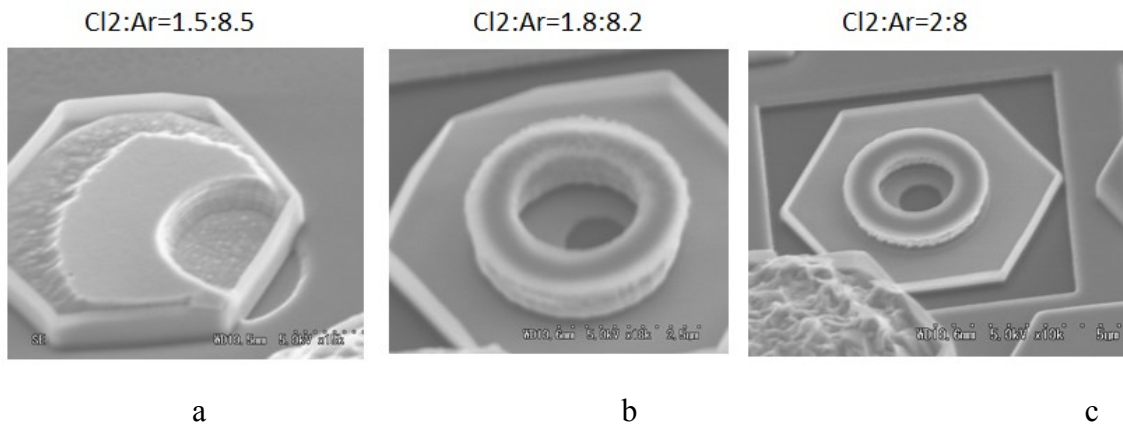
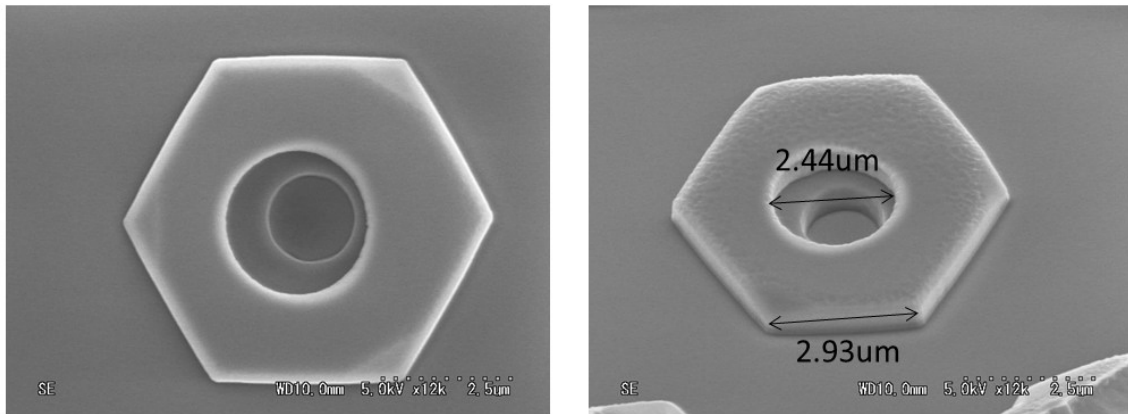


Fig. 4-7 InGaAs Etching dependence to ratios of Cl2.

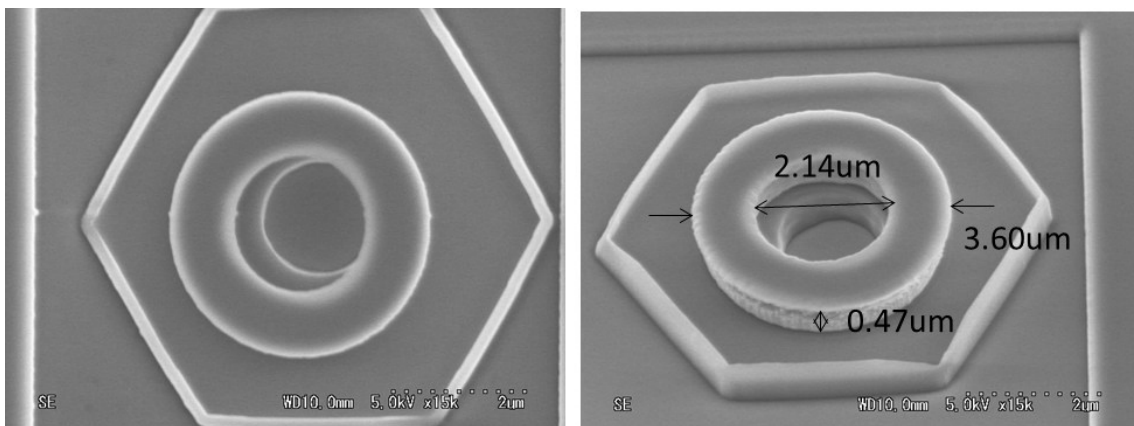
Usually Cl2 plays the role of isotropic etching. Abundance in Cl2 may increase susceptibility to undercut. Otherwise, it means that Cl2 is not enough, such as in Fig. 4-7(a). Based on the etching result of current recipe, we are able to tune the Cl2/Ar ratio one step closer to the optimization.

4.4 Result

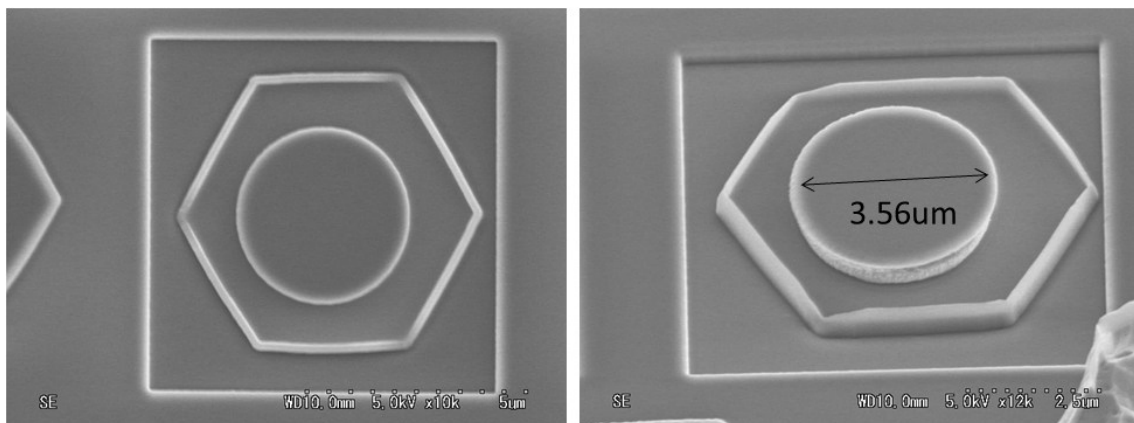
Finally, the optimized recipe applied to the real fabrication of our samples.



a



b



c

Fig. 4-8 InGaAs microdisk cavities integrated on Si (a)hollow hexagonal cavity (b)ring cavity (c)circular disk cavity

The white hexagonal walls in ring and circular disk are the residue of sputtering SiO₂. After InGaAs is etched away, they remain to be there. There is a little misalignment here due to the issues mentioned in alignment. In addition, the diameter of the outer circle is

0.4 μm (10%) smaller than the designed value (4 μm), due to the deviation introduced in EB writing and dry etching. Except these, we think that our fabrication is successful.

Chapter 5 Photoluminescence measurement

In this chapter we will first introduce the PL system in our lab, and then demonstrate the photoluminescence characteristics of hollow hexagon cavity, ring cavity and circular disk cavity in room temperature.

5.1 PL system

PL system consists of 532nm CW laser, objective lens, steering stage and gratings and PyLoN sensor. Graded neutral density filter is set in front of laser to tune the intensity of pumping light. It is connected to a motor so that we can control the pumping without restarting laser. Four kinds of magnification (5x, 20x, 50x, 100x) for objective lens can be chosen to locate the device and adjust the spot size on stage. Steering stage can be controlled by either remote controller or command in computer with specific coordinates. Camera is connected with a CCD screen, where we can see the device and spot of pumping light with proper adjustment. There is a convertible part in the steering stage. It enables us to switch from the sample holder or another stage with fiber in the center. Latter should be used to align the optical path at setup. The excited light from sample goes together with pumping light through objective lens, passing a green light filter, where the pumping light is blocked. Grating enables us to separate the excited light into different wavelengths, which will be detected by the PyLoN respectively. There are center wavelength and grating options, we can choose where the grating and sensor works and specify the wavelength range we are interested in. Here we have to notice that PyLoN sensor in our lab has a cutoff at the wavelength of 1.58 μ m. It means that it is incapable to detect spectrum wavelength larger than 1.58 μ m.

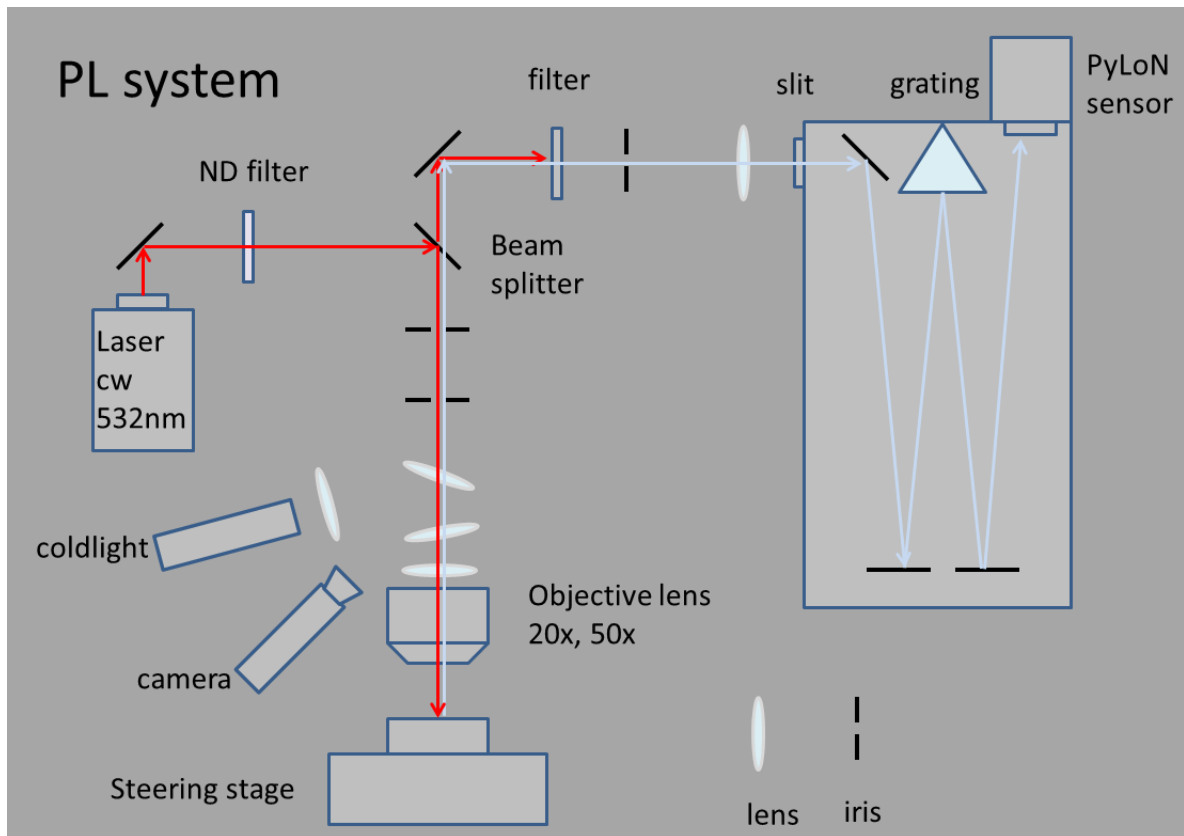


Fig. 5-1 Photoluminescence system

5.1.1 Setup

During the setup, we should set the stage with fiber instead of sample holder. First we confirm the optical path from laser to the stage, by adjusting the lens and iris in between. Second, we set one red light source to fiber, which represents the excited light from device. The red light should go exactly the same way passing the iris. Third, we set the optical path before the grating. Fourth, replace the red light source with a signal generator, which can do sweep with a wide range of wavelength. Adjust the lens in front of the slit so as to get the same response from PyLoN sensor. Usually some sort of selectivity can be observed, which means that sensor detects different intensity at various wavelengths despite of same power at input. It cannot be eliminated, but can be improved with minor adjustment.

5.1.2 Basic flow of measurement

After setup and some tests with signal generator, we change steering stage with sample holder. Before measurement, PyLoN sensor will be cooled down with liquid Nitrogen to reduce the noise. It will be locked up at the temperature value we set (usually -90°C).

When the setting temperature is reached, we turn on cold light and camera to check the location of device. There is a weak spot emitted from laser and passing graded ND filter. Steering stage can be controlled by remote controller in x, y, z direction to make this spot coincide with our device. However, we need to confirm this information with hyperspecx and hyperspecy, which do scanning in x and y direction in the vicinity of the original point. Each scanning consists of several steps of PL measurement. For example, we can set range 40um and step 1um, which will give us 41 PL measurement results plotted in the same picture. Exact coordinates can be extracted from this information. As we move pumping light to our device, we can do scanning in z direction to optimize the beam waist, where the highest intensity per area lies. After this, we can do 2D scanning with fine resolution. It will give all the spectrums at different place of the device. Pumping power could be increased for further analysis.

Lens refer to microscope lens, with magnification of 20x and 50x. M plan Apo NIR. Thorlab.

magnification	W.D. [mm]	f [mm]
20x	20	10
50x	17	4

Table. 5-1 Lens properties

Theoretically, the beam waist of the output after the lens has linear relationship with focal lens, if we consider Gaussian beam at the input. By switching the lens to 20x, we can increase the spot size by 2.5 times.

5.2 Result

We take PL measurement of sample 6b (with 1um SiO2 mask). The pumping power is set to be 0 dBm in the 2D scanning, sensor temperature locked at -90°C, 500ms exposure time, center wavelength is set to be 1520nm, grating coarse. 2D scanning depicts light intensity of whole scanning area at specific wavelength, and spectrum depicts light intensity of whole wavelength at specific spatial coordinate.

5.2.1 InGaAs island

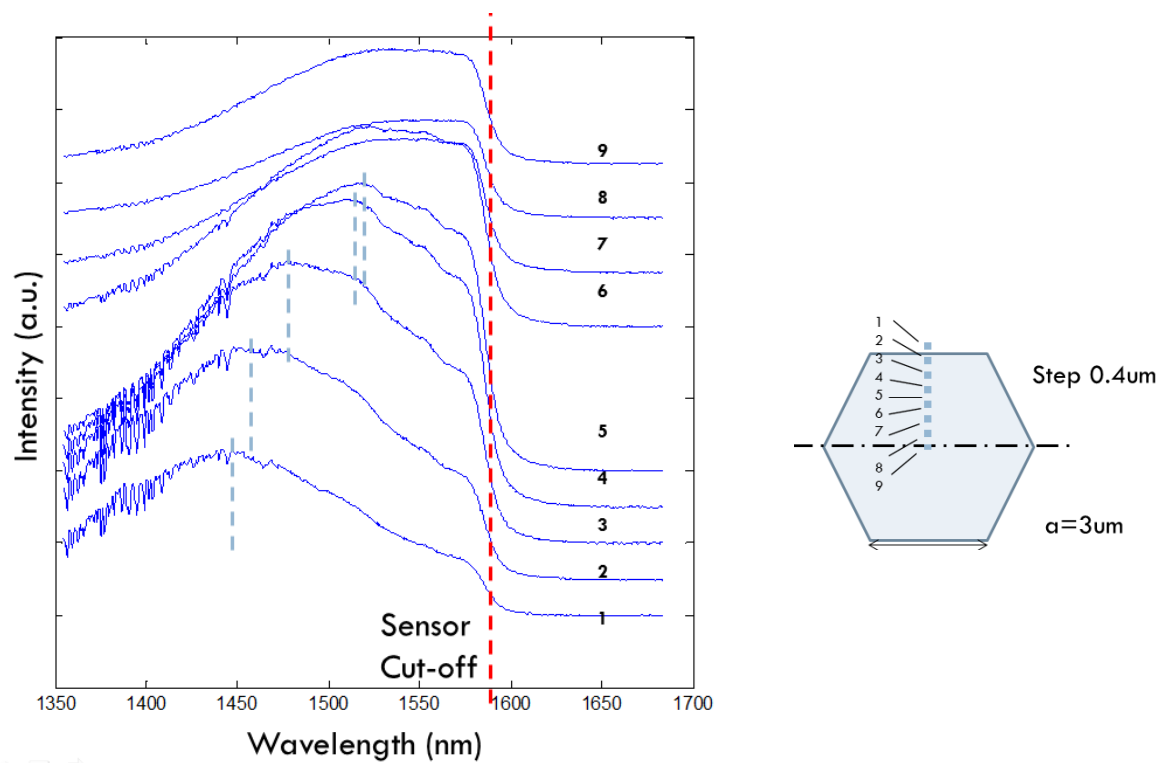


Fig.5-2 PL Spectrum from edge to center in InGaAs hexagonal island

From Fig.5-2, strong photoluminescence is observed at 1550nm wavelength range at this material. Obvious red-shift in wavelength is demonstrated as the scanning spot moving from edge to center of InGaAs hexagonal island. As we know that luminescent wavelength is related to the band-gap of InGaAs(Fig.5-3), therefore we can deduce the Ga composition in InGaAs.

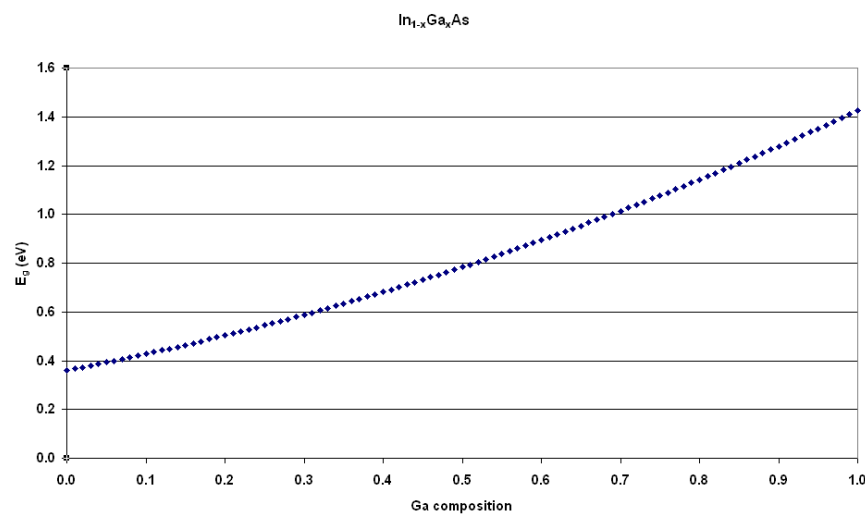


Fig. 5-3 InGaAs Band-gap dependence to Ga composition

$$\lambda_{\text{In}_{1-x}\text{Ga}_x\text{As}} = \frac{h \cdot c}{E_g}$$

Emission peak is in the range of 1.45 μm to 1.57 μm , suggesting Ga composition at the peak to be near 50% to 53%.

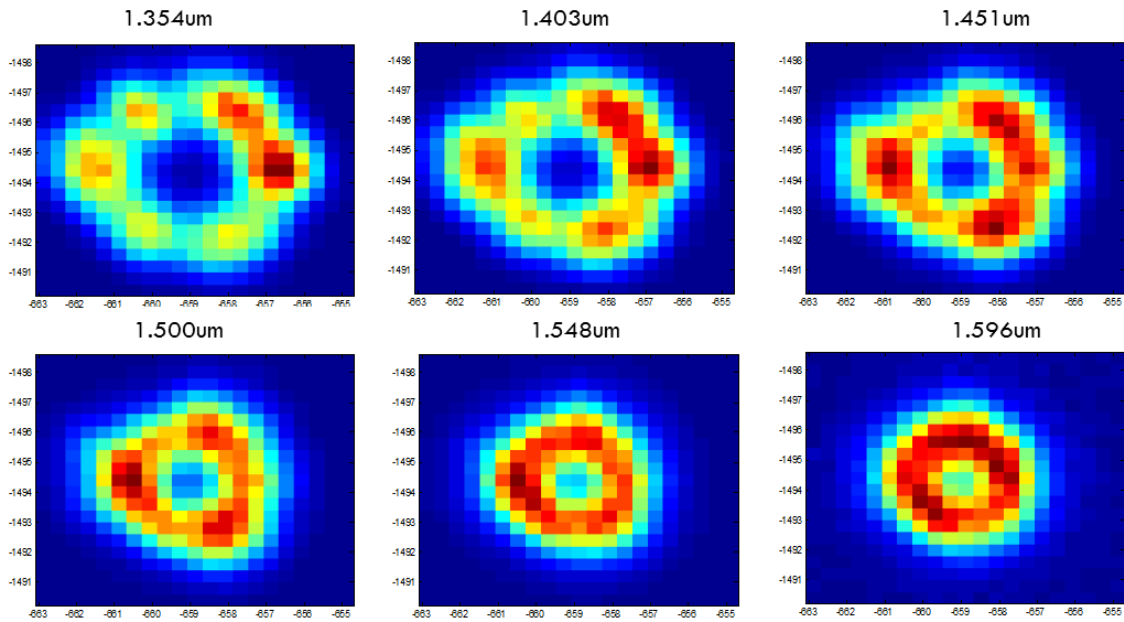


Fig. 5-4 2D scanning PL response of InGaAs island at different wavelength

By scanning the $8\mu\text{m} \times 8\mu\text{m}$ square with step of $0.4\mu\text{m}$, we can get the PL spectrum at 441 points. Each spectrum consists of intensity against wavelength at one coordinate. If we choose certain wavelength and depict the intensity at all coordinates, we can have 2D scanning PL response at certain wavelength. Fig. 5-4 shows 6 PL responses at different wavelength with binning of 50nm . Light intensity changes from weak to strong as the color from blue to red.

From this information we find weak PL response in the center of InGaAs disk. Due to the growth scheme, the center part is mainly InAs. It has relatively low band-gap, emitting light at long wavelength. Besides, carriers generated by pumping at InGaAs region can flow to low band-gap InAs region, resulting in long-wavelength emission. Therefore the removal of InAs is necessary.

In the short wavelength range, $1.35\mu\text{m}$ to $1.40\mu\text{m}$ for example, we can recognize the hexagonal structure very well. Some bright spot positioned in the angle of hexagon can be seen, showing intense emission of light there. In the wavelength range of $1.45\mu\text{m}$ to $1.6\mu\text{m}$, we notice that the emission area shrinks to the center of the cavity, and losing

the cavity property of hexagon. It resembles more to triangle. The triangle resemblance can possibly mean the Ga composition does not increase at same rate in all directions, instead it has its own selectivity. We can notice the ending lines at the three angles. It is reasonable for crystal growth has selectivity in directions, but the inhomogeneity of Ga composition can hurdle the layer properties. If we design a ring cavity on this material, it cannot be taken as the homogeneous material as we set in FDTD simulation.

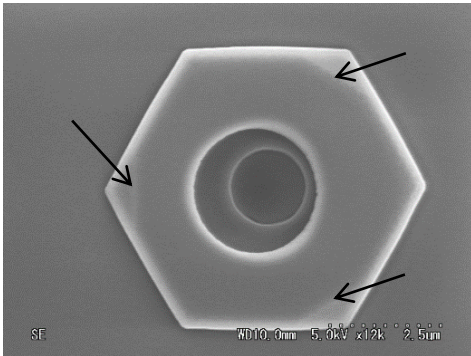


Fig. 5-5 Growth ending lines at the three angles of InGaAs. (Ignore the hollow shape)

5.2.2 Hollow hexagonal cavity

The PL properties of raw InGaAs island is introduced in last section, in this section we will demonstrate the PL results in hollow hexagonal cavity.

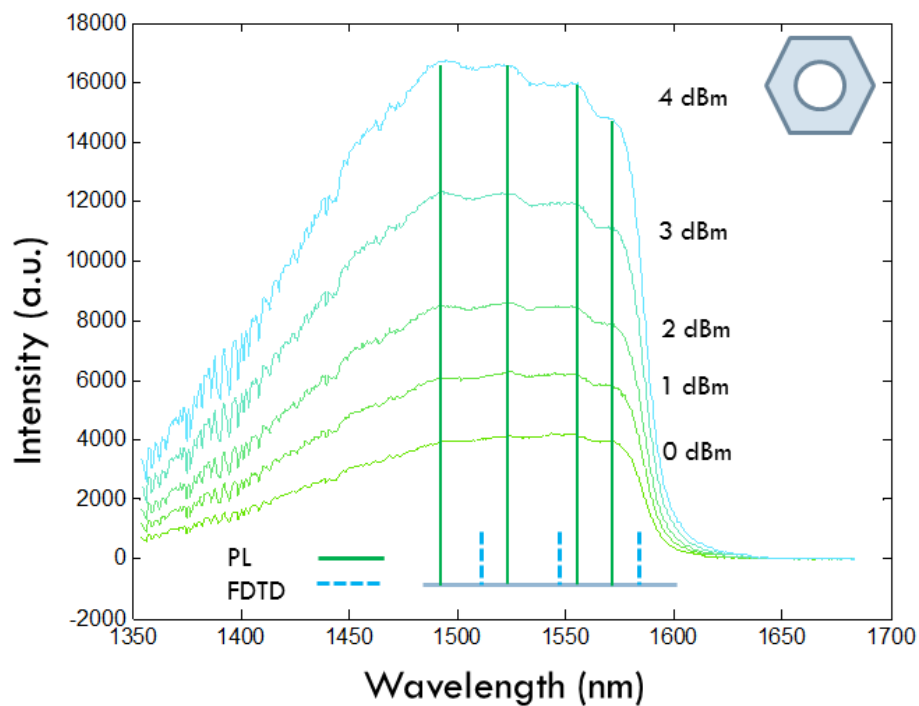


Fig. 5-6 PL spectrum at different pumping power in hollow hexagonal cavity

By etching suitable hole at the center of InGaAs hexagon, we have observed PL result suggesting the resonant properties of a cavity. Fig. 5-6 shows the PL spectrum at different pumping power from 0dBm to 4dBm, several resonant peaks begin to emerge at power 1dBm. The FSR (free spectrum range) between adjacent peaks turns out to be near 30nm. And based on FDTD simulation at the same geometry, it has FSR near 35nm. Their FSR is very close even though the resonant wavelength doesn't coincide together perfectly. We think that this is strong evidence representing the resonant properties of this cavity.

Fig. 5-7 shows 8 μm *8 μm scanning image of hollow hexagonal cavity with step of 0.4 μm . It is for simplicity that every 50nm binning is taken to give a glimpse of the light field distribution at different wavelength range. Light intensity changes from weak to strong as the color from blue to red.

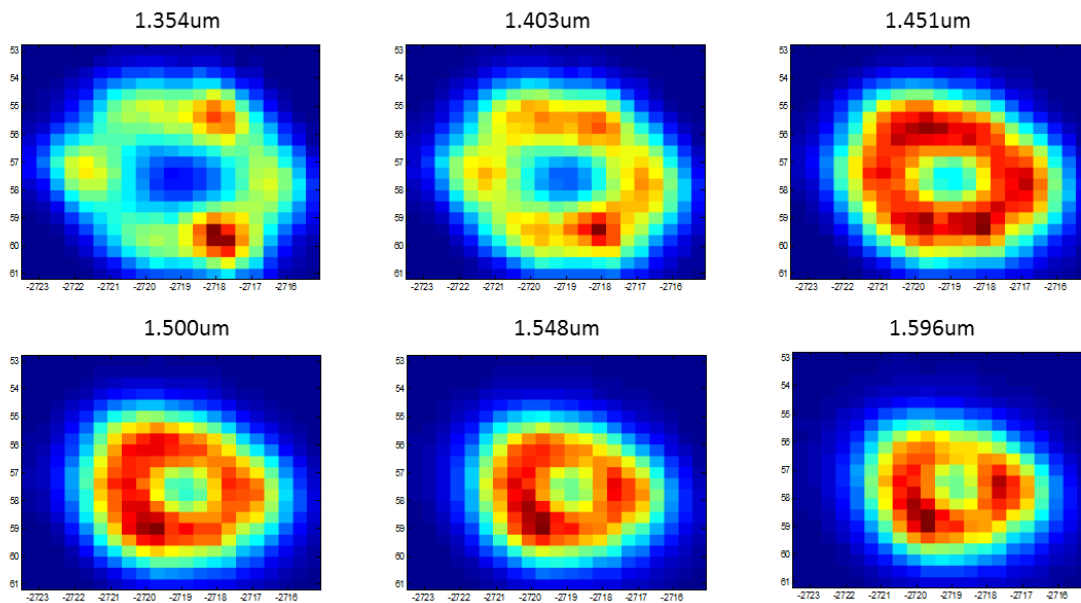


Fig. 5-7 2D scanning PL response of hollow hexagonal cavity with 50x lens at different wavelength

From figure above we find that it has similar PL response with raw InGaAs island, but actually the center part has been completely removed.

We have introduced the size of microscope lens in last sections. By switching the lens magnification to 20x, larger spot size can be obtained. If the cavity is not fully pumped, it will lower the possibility of resonance. For comparison, we have also take PL measurement of hollow hexagonal cavity with larger spot size. The data is demonstrated

in Fig. 5-8.

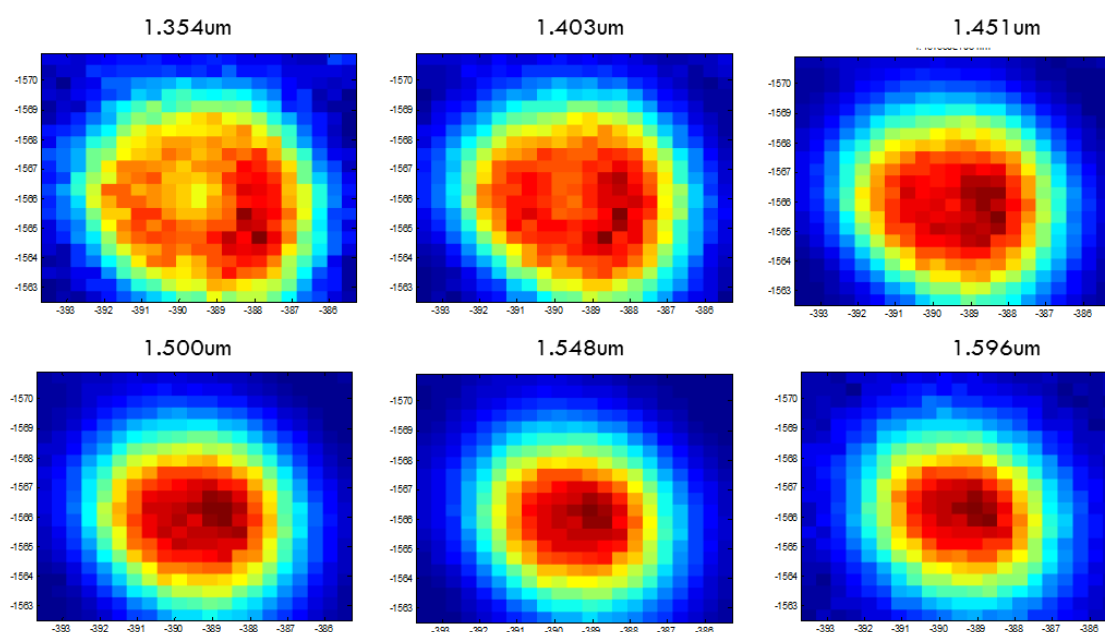


Fig. 5-8 2D scanning of InGaAs hollow hexagonal cavity with 20x lens at different wavelength

We find that previous non-radiative region in the center of the cavity is replaced by the highest intensity of light emission, based on 2D scanning image. In addition, the emission region has increased. It means that the spot size is bigger and the lens collects information as a whole unit instead of each point in hollow hexagonal cavity. Similar resonant peaks can be observed under this spot size.

5.2.3 Ring cavity

Following the same experiment procedure, we will demonstrate the PL result of ring cavity and disk cavity here.

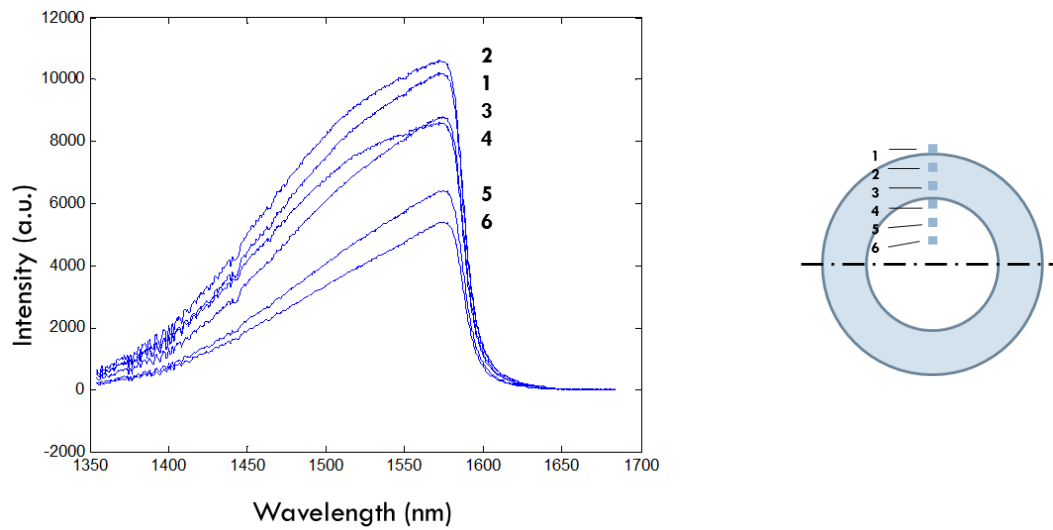


Fig. 5-9 PL Spectrum from edge to center in InGaAs ring cavity

From Fig.5-9, strong photoluminescence is observed at 1550nm wavelength range. It is very broad, and keeping increasing in intensity as it move to long wavelength. As we mentioned before, there is cut-off of this sensor, so we cannot derive resonant information from this figure. The only conclusion here is that the resonant peak should be larger than this cut-off. However, it shows very uniform PL spectrum as the scanning spot moving from edge to center of InGaAs ring. According to the SEM in chapter 4, ring has width of 0.8 μ m. It means that only two spots can be right on the InGaAs material during the scanning when the scanning step to be 0.4 μ m. From this we can see that the spot size is actually larger than we assumed. In this case it is large enough to collect the spectrum information at the center of the ring. With 20x lens, we can detect only similar spectrum as in Fig. 5-9

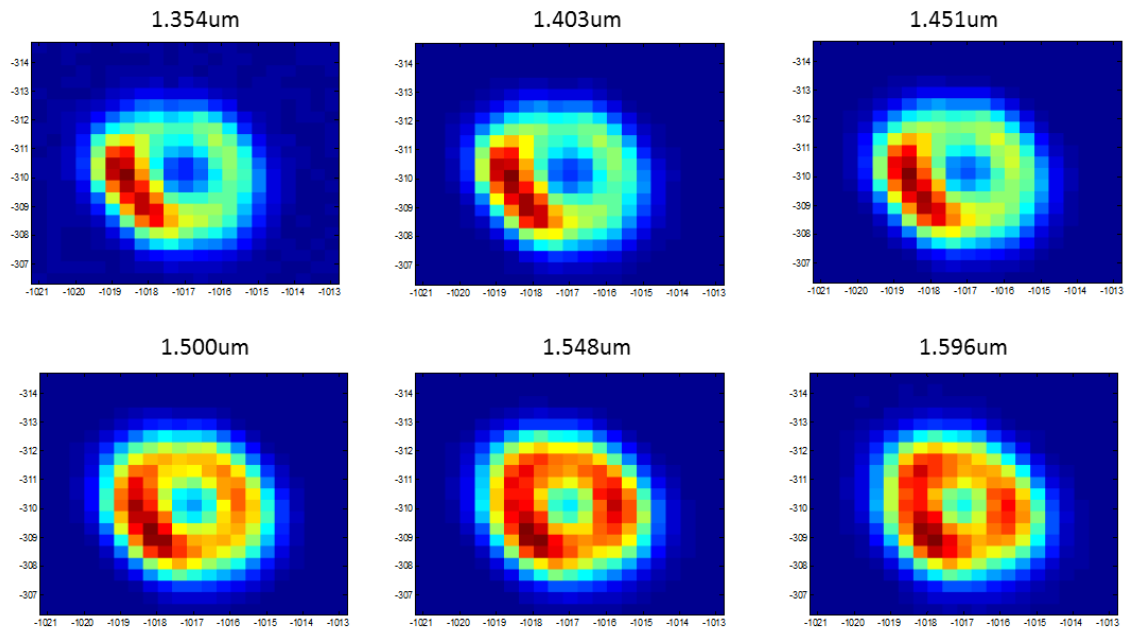


Fig. 5-10 2D scanning PL response of InGaAs ring cavity of area1_8_10_ring3 with 50x lens at different wavelength

Fig. 5-10 shows the 2D scanning image at different wavelength. Ring shape can be recognized with ease. At short wavelength, some intense spots can be seen at the left of the ring. We still do not fully understand the inhomogeneity of the PL response here. It could be some issue of crystal quality, or some defects at the surface.

5.2.4 Circular disk cavity

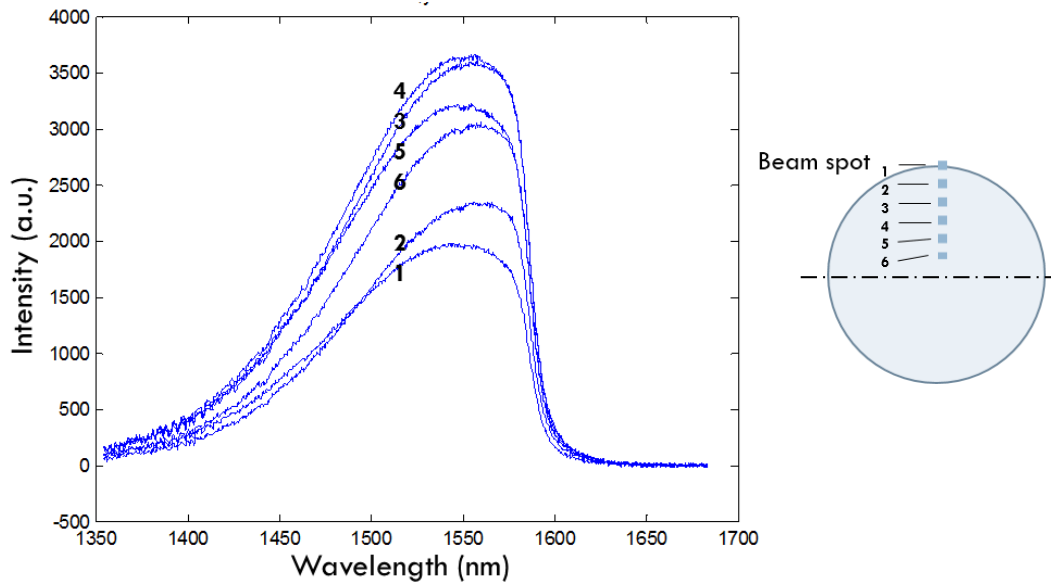


Fig. 5-11 PL Spectrum from edge to center in InGaAs circular disk cavity

Fig. 5-11 it shows similar peak wavelength of PL spectrum as the scanning spot moving from edge to center of InGaAs disk. The central peak is about 1.55 μ m.

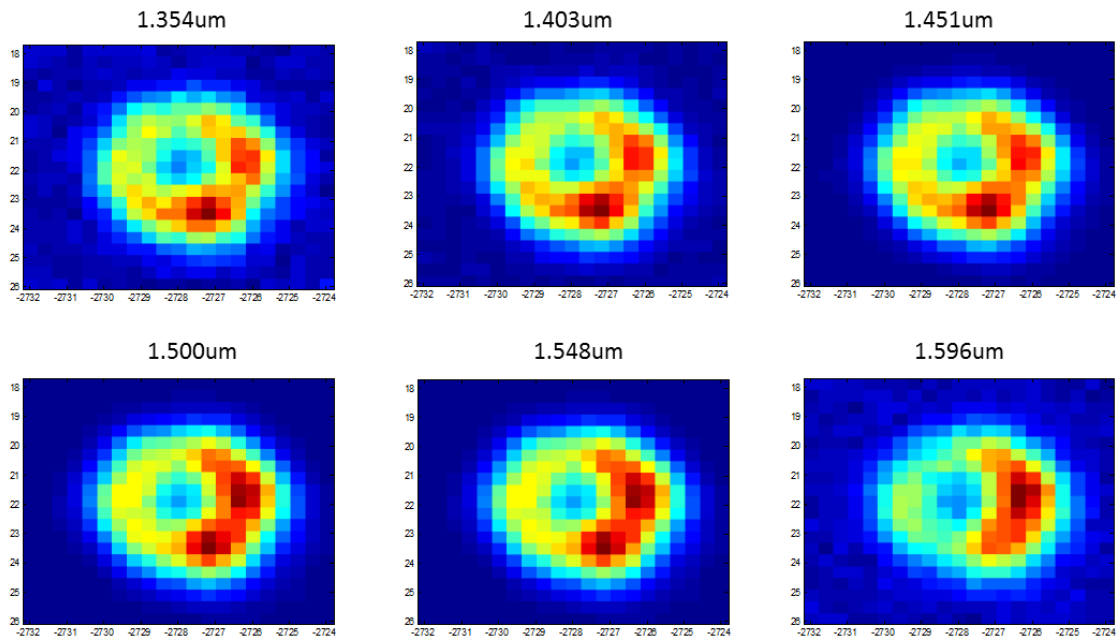


Fig. 5-12 2D scanning of InGaAs circular disk cavity of area2_6_1_disk at different wavelength

In Fig. 5-12, similar 2D PL response is observed with ring cavity. Non-radiative region

can be seen due to the InAs in the center.

To elucidate the effects in resonant wavelength introduced by the shape of cavities, we compare raw material (green), ring cavity (blue) and circular disk (red) with their respect PL spectrum together in Fig. 5-13. The spot taken in raw material is 2 μ m away from island center to make a fair comparison.

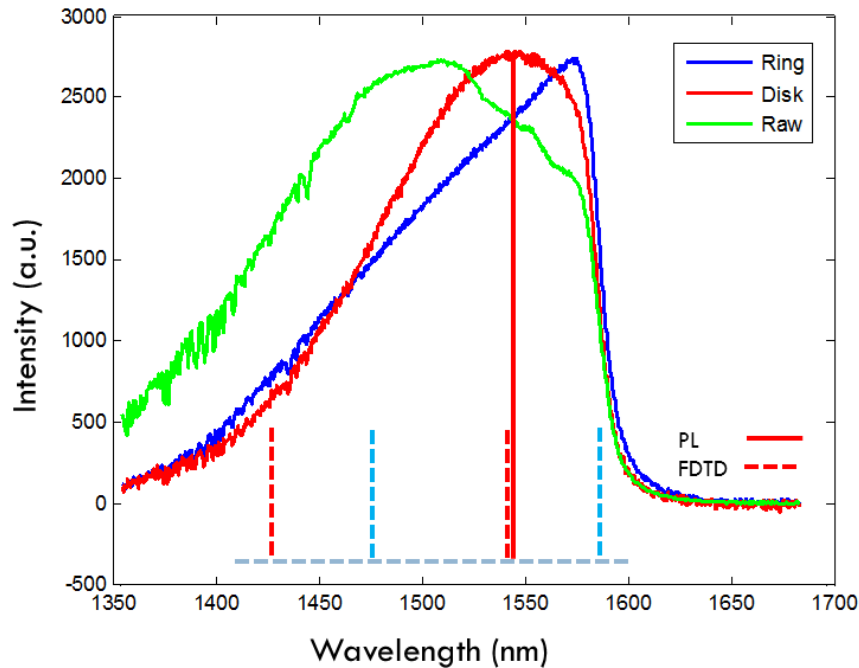


Fig. 5-13 Normalized PL spectrum of ring and circular disk cavity compared with raw material

As shown in Fig. 5-13, the ring cavity and disk cavity have a red-shift in peak wavelength in PL spectrum, compared with raw material. In particular, circular disk structure has a peak near 1540nm, which fit with simulation result very well. Even though influenced by the cut-off of the sensor, ring cavity exhibits higher resonant wavelength than the ring. Given the specific geometry in this case, the FDTD simulation suggests that ring structure has resonant peak around 1470nm and 1580nm. If we recall here that ring and circular disk have the same outer radius, which means that they should have similar PL spectrum, in terms of material. Therefore we conclude that cavity properties have played roles in the red-shift of resonant peak. The cavity resonance enforces the ring structure having higher resonant wavelength than the disk. Multiple resonant peaks are not observed not only by the limitation of the sensor dynamic range, but also by the relative large FSR, compared with hollow hexagonal structure.

In terms of repeatability, several devices on the same sample have been measured. They have very similar PL spectrum. But due to the location and variation in each device, we cannot expect the same PL result in each measurement. For example, in some ring structure, we have PL spectrum below

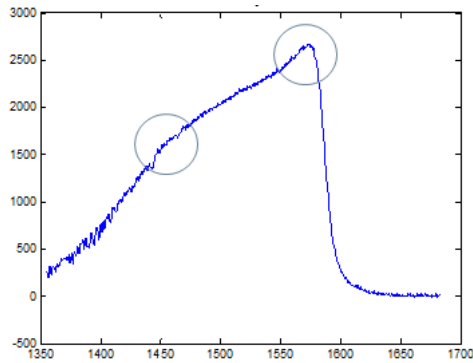


Fig. 5-14 PL spectrum of 6b_area2_6_1_ring1

The second twist in this figure can be possibly associated with resonant wavelength around 1470um.

5.3 Summary

We have taken PL measurement to our samples, including hollow hexagon, ring and circular disk, with 50x and 20x magnification. We have observed emission of InGaAs at wide range of wavelength. Several peaks associated with resonance in cavity are observed in hollow hexagonal cavity. It has similar FSR compared with FDTD simulation result. In addition, we have shown the PL spectrum of ring cavity and disk cavity. Despite their high Q factor in simulation, only broad spectrum is observed. Compared with raw material, the resonant properties of ring and disk have a red-shift effect in peak wavelength. We conclude that cavity properties have played roles in the red-shift of resonant peak. The cavity resonance enforces the ring and disk cavity having higher resonant wavelength than the island. It is consistent with FDTD simulation. Multiple resonant peaks are not observed not only by the limitation of the sensor dynamic range, but also by the relative large FSR. Lasing has not been observed.

Chapter 6 Summary

Towards III-V integrated lasers on Si substrate, in this thesis we have proposed three types of microdisk structures, including hollow hexagonal cavity, ring cavity and circular disk cavity on InGaAs material. Their characteristics have been analyzed numerically and experimentally.

We have achieved drastic improvement in uniformity and quality of InGaAs island on Si with 1 μ m thickness SiO₂ mask by MC-SA MOVPE growth. This is the crucial technique which allows monolithic integration of III-V on silicon for optical device. The InGaAs hexagon can be the material for further cavity design and fabrication.

By 3D FDTD simulation, we demonstrate that by simply etching a hole with a suitable radius at the center of hexagonal disk, quasi-WGM appears and Q factor improves drastically. In addition, ring and circular disk cavity have extreme high Q factor at certain size. Their dependence to geometrical size and mode transition are demonstrated.

Based on the information in simulation, we have successfully fabricated three types of cavities on InGaAs material.

In PL measurement, several peaks associated with resonance in cavity are observed in hollow hexagonal cavity. Compared with raw material, the resonant properties of ring and disk have red-shift effect in peak wavelength. All these information suggests that cavity properties have been observed. But somehow lasing has not been observed. Some issues associated with fabrication and measurements are discussed below.

On the fabrication aspect, in spite of the improvement in MC-SA InGaAs growth, the crystal quality of InGaAs has not been fully investigated. Based on PL result, some inhomogeneity of Ga component and selectivity in growth direction can affect the material platform itself. As our ultimate goal is the realization of electrical pumping lasing in this platform, other issues including doping should be implemented. Besides, alignment can be improved by redesign the alignment mark. In terms of yield, ring cavity and circular disk cavity are superior to hollow hexagonal cavity, as they have relatively large tolerance in alignment. Based on FDTD simulation, these structures employ their circular shape to have high Q whispering gallery mode. While in terms of sidewall roughness, the hollow hexagonal cavity has its advantage as it can employ the

natural hexagonal facet of InGaAs island. Therefore several tradeoffs are presented here. If we want shape with high Q, ring cavity is the best choice. It can also give a high yield in fabrication. But the Q factor can be compromised by the roughness at the sidewall, based on the dry-etching condition of InGaAs. If we want good confinement at the sidewall, hollow hexagonal cavity can be an interesting approach, though it may suffer from offset in alignment and relatively moderate Q factor.

On the measurement aspect, the most important problem we consider is the spot size of PL system. If the spot area is too small to cover the whole device, partially excited carriers may not be sufficient to support the lasing mode in such cavity. Switch the lens to magnification of 20 from 50 has merit to enlarge the spot size by 2.5 times. But even in that case we failed to observe extra information of resonance. Pinhole to reduce the beam width at the pumping side is not taken for safety consideration. Furthermore, low temperature PL measurement can be implemented.

Having full compatibility with the MC-SA MOVPE method, the presented scheme could be an attractive approach toward the monolithic integration of InGaAs microdisk lasers on silicon platforms.

Reference

- [1] L. P. D. J. Lockwood, *Silicon Photonics*, 2004.
- [2] D. A. B. Miller, "Device requirements for optical interconnects to silicon chips," *Proc. IEEE*, vol. 97, pp. 1166-1185, 2009.
- [3] G. Chen, H. Chen, M. Haurylau, N. A. Nelson, D. H. Albonese, P. M. Fauchet, *et al.*, "Predictions of CMOS compatible on-chip optical interconnect," *Integration-the Vlsi Journal*, vol. 40, pp. 434-446, Jul 2007.
- [4] J. Liu, X. Sun, R. Camacho-Aguilera, L. C. Kimerling, and J. Michel, "Ge-on-Si laser operating at room temperature," *Opt. Lett.*, vol. 35, pp. 679-681, 2010.
- [5] L. Liao, A. Liu, D. Rubin, J. Basak, Y. Chetrit, H. Nguyen, *et al.*, "40 Gbit/s silicon optical modulator for highspeed applications," *Electronics Letters*, vol. 43, pp. 1196-1197, Oct 2007.
- [6] C. Gunn, "CMOS photonics for high-speed interconnects," *Ieee Micro*, vol. 26, pp. 58-66, Mar-Apr 2006.
- [7] A. Biberman and K. Bergman, "Optical interconnection networks for high-performance computing systems," *Reports on Progress in Physics*, vol. 75, p. 15, Apr 2012.
- [8] H. Rong, "Low-threshold continuous-wave Raman silicon laser," *Nature Photon.*, vol. 1, pp. 232-237, 2007.
- [9] J. Liu, "Tensile-strained, n-type Ge as a gain medium for monolithic laser integration on Si," *Opt. Express*, vol. 15, pp. 11272-11277, 2007.
- [10] M. E. Groenert, "Monolithic integration of room-temperature cw GaAs/AlGaAs lasers on Si substrates via relaxed graded GeSi buffer layers," *J. Appl. Phys.*, vol. 93, pp. 362-367, 2003.
- [11] D. Liang, "Hybrid silicon ($\lambda=1.5$ μm) microring lasers and integrated photodetectors," *Opt. Express*, vol. 17, pp. 20355-20364, 2009.
- [12] 赤坂勇, *III-V族化合物半導体*: 倍風館.
- [13] R. Chen, T.-T. D. Tran, K. W. Ng, W. S. Ko, L. C. Chuang, F. G. Sedgwick, *et al.*, "Nanolasers grown on silicon," *Nature Photonics*, vol. 5, pp. 170-175, Mar 2011.
- [14] G. Roelkens, D. Van Thourhout, R. Baets, R. Notzel, and M. Smit, "Laser emission and photodetection in an InP/InGaAsP layer integrated on and coupled to a silicon-on-insulator waveguide circuit," *Opt. Express*, vol. 14, pp. 8154-8159, 2006.
- [15] A. W. Fang, "Electrically pumped hybrid AlGaInAs-silicon evanescent laser," *Opt. Express*, vol. 14, pp. 9203-9210, 2006.
- [16] A. W. Fang, E. Lively, Y. H. Kuo, D. Liang, and J. E. Bowers, "A distributed feedback silicon evanescent laser," *Opt. Express*, vol. 16, pp. 4413-4419, 2008.
- [17] A. W. Fang, B. R. Koch, R. Jones, E. Lively, D. Liang, Y.-H. Kuo, *et al.*, "A Distributed Bragg Reflector Silicon Evanescent Laser," *Ieee Photonics Technology Letters*, vol. 20, pp.

- 1667-1669, Sep-Oct 2008.
- [18] T. Spuesens, "Improved design of an InP-based microdisk laser heterogeneously integrated with SOI," *Proc. 6th IEEE Int. Conf. Group IV Photon.*, pp. 202-204, 2009.
 - [19] G. Roelkens, L. Liu, D. Liang, R. Jones, A. Fang, B. Koch, *et al.*, "III-V/silicon photonics for on-chip and inter-chip optical interconnects," *Laser & Photonics Reviews*, vol. 4, pp. 751-779, Nov 2010.
 - [20] S. M. Grist, S. A. Schmidt, J. Flueckiger, V. Donzella, W. Shi, S. T. Fard, *et al.*, "Silicon photonic micro-disk resonators for label-free biosensing," *Optics Express*, vol. 21, pp. 7994-8006, Apr 8 2013.
 - [21] A. C. Tamboli, E. D. Haberer, R. Sharma, K. H. Lee, S. Nakamura, and E. L. Hu, "Room-temperature continuous-wave lasing in GaN/InGaN microdisks," *Nature Photonics*, vol. 1, pp. 61-64, Jan 2007.
 - [22] L. Rayleigh. (1914) *Philos. Mag.*
 - [23] M. Deura, Y. Kondo, M. Takenaka, S. Takagi, Y. Nakano, and M. Sugiyama, "Twin-free InGaAs thin layer on Si by multi-step growth using micro-channel selective-area MOVPE," *Journal of Crystal Growth*, vol. 312, pp. 1353-1358, APR 1 2010 2010.
 - [24] A. H. Y. Fujimoto, J. O. Kjellman, S. Watanabe, M. Sugiyama, and Y. Nakano, "Photoluminescence of InGaAs Islands on Si(111) Substrate Grown using Micro-Channel Selective-Area MOVPE," presented at the Optical MEMS & Nanophotonic Conference 2012.
 - [25] M. Deura, T. Hoshii, T. Yamamoto, Y. Ikuhara, M. Takenaka, S. Takagi, *et al.*, "Dislocation-Free InGaAs on Si(111) Using Micro-Channel Selective-Area Metalorganic Vapor Phase Epitaxy," *Applied Physics Express*, vol. 2, JAN 2009 2009.
 - [26] M. Sugiyama, Y. Kondo, M. Takenaka, S. Takagi, and Y. Nakano, "Uniformity improvement of selectively-grown InGaAs micro-discs on Si," *Journal of Crystal Growth*, vol. 352, pp. 229-234, Aug 1 2012.
 - [27] Y. Kondo, M. Deura, Y. Terada, T. Hoshii, M. Takenaka, S. Takagi, *et al.*, "Initial growth of InAs on P-terminated Si(111) surfaces to promote uniform lateral growth of InGaAs micro-discs on patterned Si," *Journal of Crystal Growth*, vol. 312, pp. 1348-1352, Apr 1 2010.
 - [28] K. S. Yee, "NUMERICAL SOLUTION OF INITIAL BOUNDARY VALUE PROBLEMS INVOLVING MAXWELLS EQUATIONS IN ISOTROPIC MEDIA," *Ieee Transactions on Antennas and Propagation*, vol. AP14, pp. 302-&, 1966 1966.
 - [29] L. He, S. K. Oezdemir, and L. Yang, "Whispering gallery microcavity lasers," *Laser & Photonics Reviews*, vol. 7, pp. 60-82, Jan 2013.

List of publications

International

Yufeng Fu, Baifu Zhang, Jon Øyvind Kjellman, Takuo Tanemura, and Yoshiaki Nakano
“Numerical Study on Hollow Hexagonal InGaAs Microdisk Laser on Silicon”, CSW
IPRM, Montpellier France, May 2014.

List of equipment

Oxidation furnace

EB writer: ADVANTEST F5112(Takeda vdec)
CRESTEC CABL-9200TFTN

Sputterer ANELVA E-200S

ICP-RIE ANELVA L-201D-SLA

MOVPE1 AIXTRON

SEM Hitach S-4300

Confocal microscope Lasertec H1200

PL system Thorlabs

Acknowledgement

It has been two years since I stepped into U of Tokyo. And I have enjoyed the productive life here.

I would like to express my sincere gratitude to my supervisor Prof. Y. Nakano for kind invitation and constant encouragement. I greatly appreciate insightful guidance and comments from Prof. T. Tanemura about my cavity design and PL measurement. Besides, I deeply thank Prof. M. Sugiyama for his valuable ideas and comments about MOVPE growth. In addition, I would like to thank Kubota sensei for the instructions and advices on EB lithography and wafer dicing in Takeda. Constructive comments from Watanabe sensei and Higo sensei have also helped me a lot.

I would like to thank all the members of Nakano laboratory for valuable and meaningful discussions. I am very grateful to Jon-san for instructions on almost every aspect of my research. Wang-san, Tohma-san and Kondo-san have shared their valuable comments on InGaAs MC-SA MOVPE growth. In fabrication, I have learned a lot from Okimoto-san about ICP etcher and sputter machine. Besides, I have received instructions and comments from Fujimoto-san, Zhang-san, Cui-san, Inoue-san. I thank you all. My work can never be done without you.

Last but not least, I would like to express my thanks to my parents for their encouragement.

Yufeng Fu
August, 2014